Tietze, K., Thiel, S., Brand, K., Heinson, G. (2024): Comparative 3D inversion of magnetotelluric phase tensors and impedances reveals electrically anisotropic base of Gawler Craton, South Australia. - Exploration Geophysics, 55, 5, 575-601.

https://doi.org/10.1080/08123985.2023.2281615

Comparative 3D inversion of magnetotelluric phase tensors and impedances reveals electrically anisotropic base of Gawler Craton, South Australia

Kristina Tietze[1,2,3], Stephan Thiel[1,2], Kate Brand [1,2,4], Graham Heinson[2]

contact: kristina.tietze@gfz-potsdam.de

1 Geological Survey of South Australia, Department for Energy and Mining
2 School of Physical Sciences, University of Adelaide
3 Now at: Helmholtz Centre Potsdam - GFZ German Research Centre for Geosciences, Telegrafenberg, D-14473 Potsdam, Germany
4 Now at: Australian Space Weather Forecasting Centre, Bureau of Meteorology, Adelaide

ABSTRACT

Isotropic three-dimensional (3-D) inversion has become a standard tool in the interpretation of magnetotelluric (MT) data. 3-D anisotropic inversion codes are under development, yet the number of unknowns increases by a factor of 6 rendering the problem extremely ill-posed. Presence of anisotropy is usually inferred from (i) spurious sequences of conductive and resistive bodies or (ii) comparison with two-dimensional anisotropic modelling approaches.

Here, we investigate the 3-D structure of the Gawler Craton down to ~250 km depth using 282 sites of the AusLAMP array located in the southern half of South Australia. Inversions of the MT impedance as phase tensors and real and imaginary parts result in diverging structures at depths > 70 km. We demonstrate that a unifying model which explains all data types similarly well is suggestive of an anisotropic resistivity structure at the base of the Gawler Craton lithosphere at depths of 120-210 km. Depth location and orientation of the anisotropy agrees well with results from analysis of seismic receiver functions. We suggest that electric anisotropy in the Gawler Craton is a result of lattice-preferred orientation of olivine crystals and metasomatic processes with macroscopic preferential orientation.

Our results illustrate that inversion of phase tensor data is superior for the direct imaging of anisotropic resistivity contrasts in otherwise isotropic resistivity models; inversion models obtained with impedances may miss such structures. ‘Comparable’ overall RMS misfits are often meaningless when comparing inversion results for various data types since sensitivities differ between data types. Reliable

inversion results consistent with the entire data set can only be recovered if data fits are assessed systematically for all data representations. We also discuss the influence of error settings for phase tensors on the inversion.

Our study also revealed that, if persistent across large areas, (i) parallel orientation of phase tensor major axes, (ii) constantly high phase tensor maximum phases or (iii) diverging directions of phase tensor major axes and induction arrows are suggestive of anisotropic structures and corresponding hypotheses should be evaluated.

Keywords: Gawler Craton, LAB, Anisotropy, Magnetotellurics, AusLAMP

1 INTRODUCTION

1.1 Detecting and handling anisotropy in 3D magnetotelluric data sets

Effects of anisotropic conductivity structures on magnetotelluric (MT) transfer functions are not straightforward to assess. Different from e.g. evaluation of dimensionality of the subsurface, there is no objective, mathematical criterion to determine whether the electrical conductivity of the subsurface is anisotropic or isotropic from the measured data alone. Rather, there are several indicators of anisotropy, each of which is not a clear evidence for anisotropy on its own but which only when combined make presence of anisotropy likely. Such indicators include observations of 'phase splits' in measured data, i.e. 'large' differences of phases of off-diagonal impedances in particular towards longer periods (e.g. Heise *et al.* 2006, Häuserer & Junge 2011), alternating conductive and resistive structures in isotropic inversion models (e.g. Meqbel *et al.* 2014, Yang *et al.* 2015, Murphy & Egbert 2017, Kirkby & Duan 2019), or the inability to explain data with isotropic conductivity models (e.g. Häuserer & Junge 2011, Liu *et al.* 2019). The latter indications imply that (isotropic) modelling and inversion has been applied to the data set.

Since manifestations of anisotropy are particularly diffuse in 3D data sets, it is common procedure to treat data under the assumption of isotropic conductivity structure as long as possible. Moreover, the (isotropic) 3D MT inversion problem is computationally expensive and severely ill-posed with the number of unknowns being usually/often 10-50 times larger than the number of data points. Assuming anisotropic electrical conductivity increases the number of unknowns by a factor of 6 (three resistivities and three angles per model cell), it further complicates the modelling problem. Thus, if there is reason to assume anisotropic resistivity distribution, this hypothesis is usually tested by forward modelling tests including anisotropic features (e.g. Gatzemeier & Moorkamp 2005, Häuserer & Junge 2011, González-Castillo *et al.* 2019, Liu *et al.* 2019). Recently, several 3D inversion codes allowing for anisotropic resistivity are being developed (e.g. Cao *et al.* 2018, Guo *et al.* 2020) and their application may be useful if presence of anisotropy is suspected.

In this paper, we focus on the practitioner's perspective of the problem and present an approach on how to detect and resolve electrical anisotropy with comparative, isotropic 3D inversion of various MT data

types, applied to data collected at 282 sites across southern Australia. Anisotropic structures are described and potential explanations in the context of the regional geodynamics and geology are offered.

The analyses tie in with recent results of large-scale 3D MT inversion across the same area, which identified a conductive mantle conductor beneath the Archean-Proterozoic Gawler Craton (Thiel & Heinson, 2013, Thiel *et al.* 2018, Thiel *et al.* in prep).

1.2 Electric anisotropy in the upper mantle

Electric anisotropy in rigid materials can be a result of anisotropy within crystals as well as of macroscopic features such as fractures with preferential orientation prevailing over extended areas (e.g. Wannamaker *et al.* 2005). The lateral resolution of MT data decreases with depth. Therefore, the MT method is unable to distinguish between intrinsic/microscopic anisotropy and aligned macroscopic (cm-km) scale conductivity heterogeneities at depth (e.g. Weidelt 1999, Wannamaker 2005). Impedances and the phase tensor resolve the effective bulk resistivity of a volume rather than a point property of the material.

In the lower lithosphere / upper mantle, electric anisotropy is mainly a result of intrinsic anisotropy of the predominant mineral olivine (e.g. Gatzemeier & Moorkamp 2005, Padilha *et al.* 2006, Häuserer & Junge 2011). Characterisation of electrical conductivity of olivine has been the target of a large number of laboratory studies both on the scale of single crystals as well as for multigrain systems (see e.g. reviews of Pommier 2014, Gardés et al 2014, Yoshino & Katsura 2013). While conductivity of olivine is commonly agreed to be affected by a broad range of factors most importantly temperature, pressure, water content, grain size and grain orientation, quantification of their effects often yields disparate and sometimes contradicting results and reflects the difficulties/challenges of such laboratory measurements.

Conductivity of single crystals is found to be anisotropic in various conditions (e.g. Yoshino *et al.* 2006, Dai & Karato 2009, Poe *et al.* 2010). Measurements of Yoshino *et al.* (2006) showed lower conductivity along the [100] axis than along the other crystallographic directions at a pressure of 3 GPa (~100 km) and temperatures between 500 and 1500 K. In contrast, at 8 GPa and temperatures of 1200 °C, which are more representative of the upper asthenosphere, Poe *et al.* (2010) measured conductivities along [100] to be 2-10 times higher than along [010] and [001], in particular if water is present. For olivine

aggregates, lattice preferred orientation in the upper mantle can be expected to result in electrical anisotropy under certain conditions (Wang *et al.* 2006), but laboratory studies on strongly textured olivine samples are rare for lower lithospheric conditions. For crustal conditions and small grain sizes, Pommier *et al.* (2018) recently showed that electrical conductivity is highest parallel to the shear planes with anisotropy factors of ten or maybe higher. Overall, anisotropy factors of olivine are still poorly constrained by laboratory measurements.

Where anisotropy ratios are found to exceed that of olivine, presence of partial melt (Meqbel *et al.* 2014) or other fluids in structures with preferential orientation are considered as source of anisotropy.

1.3 Geology

The study presented here spans the extent of the Mesoarchean to Mesoproterozoic Gawler Craton (Hand *et al.* 2007, Reid *et al.* 2017, Reid 2019) and extends across the Paleoproterozoic to Mesoproterozoic Curnamona Province (Wade *et al.* 2012) in the east and the adjacent Fowler Domain (Thiel & Heinson, 2009) and Coompana Province (Pawley *et al.* 2020) in the west. The Gawler Craton has basement complexes of Meso – Neoarchean age ca. 3150 Ma granites and granite gneisses (Fraser *et al.* 2010), and ca. 2555–2480 Ma supracrustal sequences, which comprise mafic and felsic volcanics (Reid & Hand 2012, Swain *et al.* 2005). Between 2000 Ma and 1600 Ma, the Gawler Craton experienced repeated orogenesis and magmatism including the medium to high grade metamorphic Cornian Orogeny at 1850 Ma, the Kimban orogeny at 1730 Ma - 1710 Ma, and periods of igneous intrusive activity between 1690 Ma and 1580 Ma., including the 1630 Ma felsic Nuyts Volcanics and felsic to mafic-ultramafic St Peter Suite intrusions.

At 1595 Ma to 1575 Ma, the intrusive Hiltaba Suite and Gawler Range Volcanics magmatic event led to the formation of the IOCG systems in South Australia, e.g. the supergiant Olympic Dam deposit (Heinson *et al.* 2018). The magmatic event affected both large parts of the Gawler Craton and the Curnamona Province (Wade *et al.* 2012). The Gawler Craton and Curnamona Province were tectonically relatively stable until the emplacement of the Gairdner large igneous province at ~830 Ma driven by a developing rift between the two provinces (Wingate *et al.* 1998).

Pertinent to this study is the conductive Gawler Craton mantle signature first imaged through a widely spaced (~100 km) 2D array of MT data (Thiel & Heinson 2013) and further constrained through the AusLAMP MT array (Thiel *et al.* 2018). The heterogeneous mantle signature is characterised by enriched geochemical trends of the mafic magmas associated with the silicic large igneous province of the Gawler Ranges and Hiltaba Suite emplaced during the ca. 1590 Ma (Wade *et al.* 2019), including enrichment in high field strength elements, light rare earth element (LREE), negative Nb-Ta-Ti anomalies, and variable Nd isotopic compositions. The enrichment of the sub-continental lithospheric mantle is thought to originate from priming and metasomatism as a result of prior (> 1590 Ma) subduction of the Gawler Craton mantle (Skirrow *et al.* 2018, Wade *et al.* 2019).

2 MAGNETOTELLURIC DATA SET

The magnetotelluric (MT) data set considered here consists of 282 stations distributed across the Gawler Craton and its margins. Most of the data are extracted from the Australian Lithospheric Architecture Magnetotelluric Project (AusLAMP), an array of long-period MT sites that will eventually cover Australia at 0.5 degree interval (~55 km). To supplement this array, additional long-period MT sites were extracted from a variety of legacy MT surveys.

The most common transfer function of the MT method is the impedance tensor Z which relates the horizontal magnetic B and electric E field components recorded at a specific position:

$$E = ZB,$$

Where Ei and Bi are the electric and magnetic field variations recorded in north (x) and east (y) directions. Z is typically measured for a wide frequency range and contains information about the subsurface electrical conductivity structure at different depths. In 3D inversion, the tensor elements are usually considered in terms of their real and imaginary parts. Here, we also use an alternative representation of the impedance, the phase tensor Φ, introduced by Caldwell *et al.* (2004)

$$\Phi = \mathbf{X}^{-1}\mathbf{Y}$$

where X and Y are the real and imaginary part of the magnetotelluric impedance $\mathbf{Z} = \mathbf{X} + i\mathbf{Y}$. The phase tensor is derived from the observed impedance but is unaffected by galvanic distortion (Caldwell *et al.* 2004). Its invariants provide distortion-free information about the dimensionality of the underlying conductivity structure, which can be obtained directly from the observed distorted data. Phase tensor data are often visualized in terms of ellipses with size and orientation defined by the invariants of its singular value decomposition (see section A1). Booker (2013) gives a detailed review of the phase tensor and its potential for magnetotelluric data interpretation.

In addition, the vertical magnetic field component was also measured at all sites and its relation to the horizontal magnetic field is described by

$$\mathrm{Bz} = \mathbf{TB} = \mathrm{TxBx} + \mathrm{TyBy}$$

Where T is another complex transfer function usually called the induction vector. T is particularly sensitive to lateral conductivity variations.

Figure 1 shows the data as phase tensors (Caldwell *et al.* 2004) for six periods between 52 s (Fig. 1a) and 3728 s (Fig. 1f); ellipses are normalised and coloured with Φ_{max}. (cf. section A1)

For periods < 200 s (Figs 1a-b), sites located on the Gawler Craton show ellipses with low ellipticity and maximum phases between 40 and 60 degrees (greenish colours) indicating relatively homogeneous structures. Ellipses to the east and the west of the craton show high ellipticity and maximum phases below 30 degrees (dark blue colours) that illustrate a strong increase of resistivities with depth. In the period range between 300 and 1500 s (Figs 1c-e), separation of data into two regions with differing properties becomes even clearer. On top of the Gawler Craton, maximum phases usually exceed 70°, phase tensors have high ellipticity (Φ_{max}-Φ_{min} > 30°), and major axes are aligned parallel pointing on average N23°E. At the eastern and western edges of the Gawler Craton, ellipses tend to align with the craton boundaries. In contrast, stations off the Gawler Craton usually show values of 30-60° for Φ_{max} (green colours) and orientation of major axes of the ellipses varies spatially. For the longest periods > 1500 s (Fig. 1f), spatial grouping of phase tensor parameters fades out. In large parts of the survey area, Φ_{max} values are > 70° and major axis point to directions between N00° and N23°E. Only at the northernmost stations (x > 250 km in Figure 1), Φ_{max} values range between 50 and 60°.

In general, elliptical phase tensors (i.e. deviating from circular) indicate the presence of lateral conductivity variations. Ellipticity is highest close to a lateral resistivity contrast and ellipse shapes return to circular away from the contrast. Moving across a conductivity contrast, phase tensor ellipses flip orientation by 90°. On the conductive side of the contrast major axes are aligned parallel to the strike of the contrast, on the resistive side the major axis is perpendicular to the contact plane.

Notably, this data set exhibits constantly high ellipticity, high Φ_{max} values and alignment of major axes in a singular direction (~N23°E) over (i) a large, but confined region (the Gawler Craton) and (ii) persist over a wide period range (200 to 1500 s or even the longest periods). Considering this pattern of high Φ_{max} values and alignment of Φ_{max} directions, it is difficult to imagine a single conductivity contrast or isotropic body that affects data in such a homogeneous way. The data suggest presence of a lateral sequence of aligned conductivity contrasts or electric anisotropy.

Figures 2(a)-(f) show induction vectors for the same periods as phase tensors. At periods < 1000 s (Figs 2a-d), maps of real induction vectors (Parkinson convention) are dominated by a radial pattern at stations on the Gawler Craton pointing away from the craton centre towards its boundaries. This pattern persists over nearly three decades of period and suggests presence of a significant amount of conductive material located at the edges or outside the craton. The lateral extent of such conductive material does not appear to be well defined by induction vectors, since no reversal of arrow directions can be observed outside of the craton edge. In this period range, lengths of induction vectors outside the craton are often < 0.2 and orientations do not show large spatial correlation patterns. At periods > 1000 s (Figs 2e-f), the radial pattern at sites on the Gawler Craton lessens and for periods > 3000 s (Fig. 2f) most induction vectors point towards the conductive ocean to the south. A nice local feature of the data set is the reversal of induction vectors on the Eyre Peninsula (see Figs 2a-f) which persists over the entire period range. This reversal is caused by the roughly north-south trending Eyre Peninsula conductor, a known low resistivity body embedded within the Hutchison group sediments and parallel to the Kalinjala Shear Zone along the eastern part of the peninsula (White & Milligan 1984, Thiel *et al.* 2005, Curtis & Thiel, 2019, Heinson *et al.* 2022).

Notably, on the Gawler Craton induction vectors are mostly not aligned with any of the phase tensor axes. In fact, the radial pattern of induction vectors and the parallel alignment of phase tensor major

axes indicate diverging structural properties. The disparate orientations can be a result of differing sensitivity patterns. Induction vectors are particularly sensitive to lateral variations whereas phase tensors sense both lateral and vertical changes in resistivity. Moreover, penetration depths at the same period may vary between different data types. Yet, some authors interpret deviations between phase tensor axes and induction vector directions that persist over extended areas such as the Gawler Craton as a hint to anisotropy (e.g., Liu *et al.* 2019).

In the following, we perform comparative inversion of impedances as its real and imaginary parts and as phase tensors, each combined with induction arrows, to investigate if choice of the representation of impedances may influence the recovery of these particular phase tensor properties and potential anisotropic subsurface features.

3 INVERSION METHODOLOGY

3.1 Integration of a priori information and model setup

Inversion of the data set was performed in a multi-stage approach using various a priori information as shown in Figure 3. A priori information can enhance performance of 3D inversion in several ways, e.g. by providing starting models closer to the "true" solution or by narrowing the model space. In this study, we use ModEM (Egbert & Kelbert 2012, Kelbert *et al.* 2014) for inversion and forward modelling.

Here, we use phase tensors which are particularly sensitive to conductivity variations, yet have limited sensitivity to absolute resistivities of the subsurface. Starting models with resistivities close to the regional average therefore facilitate recovery of underground structures (Patro *et al.* 2013, Tietze *et al.* 2015). Thus, for stage I (Fig. 3) we derive a 1D starting and prior model from the preferred model of Thiel *et al.* (XXX), which used impedance and induction vector data for the inversion (Stage 0 in Fig. 3). In a depth range between 0 and 200 km, each horizontal layer was assigned its median of the log10-resistivities within the survey area. Model parts more than 30 km away from the outermost stations or beneath the ocean were excluded from the averaging procedure. Below 200 km, resistivities of the lowermost averaged layer were continued. Resistivities of the 1D model range between 50 and 500 Ωm. Resistivities < 200 Ωm occur in the upper 3 km, resistivities at depths ≥ 200 km measure 250 Ωm.

Resistivities of the ocean (bathymetry taken from ETOPO1 Global Relief Model, NOAA National Geophysical Data Center 2009, Amante & Eakins 2009) were set to 0.3 Ωm and fixed in inversion. Since sediments in the Great Australian Bight can reach several km thickness (Smith & Sandwell, 1997), we added a 4 km thick layer beneath the seafloor in which resistivities gradually increase with depth from 1 Ωm to the resistivity of the 1D model.

For comparison, we also tested homogeneous starting/prior models with resistivities in the range of the 1D layered model, namely 100 and 300 Ωm including ocean and sediments (not shown). The resulting inversion models did not show notable differences in resistivity structures. Yet, overall misfits and total number of iterations were slightly higher for the homogeneous models. The 1D layered starting/prior model was used both for the Gawler data set (stage Ia) and a complementary synthetic data set of a conceptual model (stage Ib) shown in the following.

Finally, in stage II we added an anisotropic feature in the deep lithosphere of the Gawler Craton (120-210 km depth) to the layered model of stage I. In the current version, ModEM only allows for isotropic resistivities in each model cell and anisotropic structures cannot be resolved in the inversion process. Hence, we simulated anisotropy by inserting a bundle of conductive lamellae into the isotropic model (e.g. Eisel & Haak 1999; cf. Gatzemeier & Moorkamp 2005, Le Pape *et al.* 2012).

Analysis of phase tensor data shows preferred alignment of phase tensor major axes at long periods and suggests (a sequence of) prominent conductivity contrasts which must be aligned over large distances. The median orientation of the major axes of phase tensor ellipses in the period range of 200 to 3750 s is N23°E. Tietze & Ritter (2013) illustrate that recovery of elongated conductive zones at depths may be inhibited if the inversion coordinate system is not aligned with strike of the conductor. Therefore, we rotated the data to N23°E. Unless stated otherwise, data and modelling are considered in this rotated coordinate system in the following.

For modelling, the survey region was discretized horizontally with a 15 km × 15 km grid. The model grid consists of 75 × 107 × 55 cells in the two horizontal and the vertical directions, respectively. The inner part comprises a uniform mesh of 55 × 87 × 55 cells with an edge length of 15 km. On all four sides, the central domain is padded with 10 planes where cell sizes increase laterally by a factor of 1.3.

The vertical thickness is 50 m for the first layer; subsequent layer thicknesses successively increase by a factor of 1.2. Based on the results of Robertson *et al.* (2020) and Thiel *et al.* (2018), we tested isotropic model covariances between 0.2 and 0.4 and finally chose a value of 0.2 and applied the covariance matrix twice for the following inversions.

3.2 Data errors

One of the most important parameters for 3D MT inversion is the choice of data uncertainties. The ModEM inversion algorithm seeks to minimise the following penalty function Ψ which consists of a data regularization and a model regularization term (Egbert & Kelbert 2012):

$$\Psi(\mathbf{m}, \mathbf{d}) = \big(\mathbf{d} - \mathbf{f}(\mathbf{m})\big)^{\mathrm{T}} \mathbf{C}_d^{-1} \big(\mathbf{d} - \mathbf{f}(\mathbf{m})\big) + \lambda \Psi_m,$$

where **d** is the observed data, **m** the resistivity model, **f**(**m**) the forward response, $\mathbf{C}_\mathrm{d}$ the data covariance, Ψ_m the model norm, and λ a trade-off parameter. The data covariance is a diagonal matrix which contains the inverse of the squared data errors e_i for each data point: $\mathbf{C}_d = diag\big(1/e_i^2\big)$. In other words, data errors describe not only the uncertainty of the data but at the same time define the relative weight of data points in the inversion process. Hence, choice of data errors and error floors does not only have to be adapted to known uncertainties of the data, but needs to account for the distribution of information to (subsets of) the data set (Tietze & Ritter 2013).

In general, MT data processing routines output uncertainties for impedance and induction vector data. Uncertainties of derived data types such as phase tensors could be obtained via error propagation schemes. In practice, uncertainties from processing are often discarded and data errors for inversion are estimated based on magnitudes (impedances) or set to constant values (induction vectors). Moreover, if data are rotated after processing to a new coordinate system, uncertainties from processing can only be used if the full error covariance matrix has been calculated. Since most processing routines only provide the variance of impedance tensor and induction vector elements, data errors for inversion usually have to be defined based on other measures.

3D inversion of impedance data and/or induction vectors is frequently used nowadays. Typical error settings for impedances use values proportional to the magnitude for off-diagonal elements (e.g., 3-10 %

of $|Zij|$) and values proportional to $|Zxy * Zyx|^{1/2}$ (e.g., 3-30 %) for diagonal impedance components (see review of Miensopust 2017, and references therein). For induction vectors errors are nearly exclusively set to constant values between 0.02 and 0.05 (e.g. Meqbel *et al.* 2014, Murphy & Egbert 2017, Liu *et al.* 2019, Tietze & Ritter 2013).

Inversion of phase tensor data has been demonstrated only with a few data sets so far (Patro *et al.* 2013, Tietze *et al.* 2015, Samrock *et al.* 2018). The study of Patro *et al.* (2013) estimated data errors from impedance variances by applying the delta method; in addition, an error floor of 10 % of $|\Phi xx * \Phi yy|^{1/2}$ was used. Tietze *et al.* (2015) used relative errors of 3 % in combination with a constant floor of 0.03. Samrock *et al.* (2018) propagated errors from impedance tensors.

For inversion of phase tensors of the Gawler data set, we compare two different approaches to defining data errors. In the first approach we used a constant error value for all data points as it is usually applied to induction vectors. We tested various values between 0.02 and 0.05 and finally chose 0.04 as the optimal value. For smaller error values, convergence is inhibited, and overall RMS values remain high. For higher values, models contain little structure and inspection of the data and model responses reveals systematic underfitting of the data which is not reflected in the RMS values. In general, using a constant value which is the same for all components results in a rotationally invariant "total" RMS when considering the full set of four components.

For the second approach, we defined data errors relative to the magnitude of the tensor elements. We chose a value of 4.24 % which corresponds to the average error when propagating errors from impedance with errors of 3 % (Fig. 4). Since elements of the phase tensors, in particular Φxy and Φyx, can be zero, we additionally applied a constant floor of 0.025.

We also inverted impedances using relative errors of 3 % in combination with an error floor of 3 % of sqrt(|Zxy*Zyx|) for the diagonal components. In all subsequent inversion runs, either phase tensor or impedance data were inverted jointly with induction vectors using a constant error of 0.03. For brevity, we refer to these joint inversions as phase tensor or impedance inversions, respectively.

For all data types, we used data at 19 periods between 10 and 3728 s. Data were inspected visually and outliers were masked manually. In addition, after some inversion runs, data points with extreme misfits

several times higher than the median normalised RMS error, corresponding to the top 1 – 3 %, were excluded from the data sets.

4 STAGE I: IS THE BASE OF THE GAWLER CRATON ANISOTROPIC?

4.1 Stage Ia: 3D inversion results of the Gawler data set

Figures 5(a)-(b) show the 3D inversion models obtained from joint inversion of phase tensor and induction vector data for the two different phase tensor error settings; Figure 5(c) displays results obtained from joint inversion of impedances and induction vectors. At depths < 100 km (first 4 panels in Figs 5a-c), structures in all resistivity models are very similar and consistent with the results of Thiel *et al.* (XXX). Outside the Gawler Craton, the uppermost 3 km comprise low resistivities (< 10 Ωm) with thicknesses of 1 – 3 km. On the Gawler Craton, sedimentary cover is usually very thin and resistivities reach 100 to > 3000 Ωm at 3 km depth. Between 3 and 14 km depth, resistivities in the entire survey area lie around 1000 Ωm. Beneath the Eyre Peninsula, a prominent conductive zone extending NNE-SSW parallel to the peninsula's eastern shore becomes visible with its top located at about 11-14 km depth. At greater depths, a ~50 km wide zone of low resistivities (1-50 Ωm) appears along the onshore edge of the Gawler Craton. To the east of the Gawler Craton, in the region of the Stuart Shelf and the Flinders Ranges resistivities are at similarly low levels. Maximum conductance can be observed between 35 and 45 km and the structure fades at a depth of 100 km. Otherwise, resistivities at these depths range between 200 and 2000 Ωm.

At depths > 100 km, structures of the models in Figures 5(a)-(c) diverge. While all models contain laterally alternating conductive (~1-5 Ωm) and resistive (~500-1000 Ωm) bodies which are oriented ~WNW-ESE, size and location of the anomalies vary. Structures extend roughly parallel to the inversion grid. Since cells in the survey area have the same length in both horizontal directions, model covariances are isotropic and sites are distributed on a close to regular grid, we do not expect significant bias from orientation of our coordinate system. Yet, we inverted the same data using a coordinate system with *x* pointing to N22°W, i.e. at an angle of 45° from the orientation shown here using the same data and modelling parameters otherwise. The models (Fig. S1) are overall consistent with the previous inversion

results; in particular, structures at depths of 100-300 km show the same orientation. Interestingly, the conductivity contrasts for both error settings (Figs S1a and S1b) are of the same magnitude. Location of the conductive and resistive units differs from previously described results of the N23°E coordinate system; conductive stripes are narrower and located "between" those of Figures 5(a) and (b).

Inversions of Figures 5(a)-(c) reached normalized RMS errors (nRMS) of 4.15, 3.46 and 4.78, respectively. Yet, since error settings between phase tensor inversions differ and relation of impedances and phase tensors is highly non-linear, nRMS cannot be used to evaluate data fit between inversions of different data types. In addition, calculating impedance responses of phase tensor inversion models in order to compare responses in terms of e.g. apparent resistivity and phase curves is not useful. Inversions of impedances may contain (small-scale near-surface) structures ("artefacts") to compensate for galvanic distortion of the impedance. The phase tensor, however, is free of galvanic distortion by definition; likewise, its inversion models are free from artefacts related to galvanic distortion. Thus, impedance responses of phase tensor inversion results are presumably close to the undistorted impedance and comparison to the measured (distorted) impedance is pointless when aiming to evaluate data fits. Instead, we opt to inspect model responses in terms of phase tensors in general.

Figure 6 compares the responses of models of Figure 5. We focus on periods > 300 s which are particularly sensitive to structures at depths > 100 km where inversion models differ. Responses at sites off the Gawler Craton are very similar and reproduce measured data very closely (cf. Fig. 1), but data fit at sites on the craton is not equivalent between the models. The best data fit on the craton is obtained for the phase tensor inversion with constant errors (Fig. 6a). Both constantly high ellipticity and Φ_{max} values are reproduced well. Figs 6(d)-(f) show that phase tensor parameters Φ_{max}, Φ_{min}, as well as the phase difference Φ_{max} - Φ_{min}, are usually reproduced within ±5°, even for extreme values. For the other two inversion results, recovery of phase tensor parameters is poorer (Figs 6b-c). While both models reproduce Φ_{max} values of > 70° in the centre of the craton, Φ_{max} decays towards the craton edges and ellipses become less elliptical. Φ_{max} values > 50° are systematically underestimated with differences of -15° on average for measured Φ_{max} > 70°; similarly phase difference Φ_{max} - Φ_{min}> 20° are increasingly underestimated (Figs 6d-f).

The findings suggest that a significant amount of conductive material at depth of 100-300 km is required to explain the data. This result is supported by forward modelling tests replacing the conductors between 100 and 300 km depth in models of Figures 5(a)-(c) by surrounding higher resistivities. Responses of the modified models cannot explain data for periods > 200 s at sites located on the Gawler Craton. In particular, Φmax values and phase differences Φmax-Φmin are underestimated by more than 20°. Sites off the craton are much less sensitive to structures at these depths, because MT signals are attenuated by thicker conductive sedimentary cover as well as by the low resistivities at the craton edges between 20 and 70 km depth.

In contrast, fit of induction vectors is comparable between each of the inversion models; also, distribution of data fits with period and site location did not reveal significant variations. Only at sites located directly at the coast, inferior data fits indicate insufficiently detailed representation of the coastline and related contrasts. In other words, the solutions of Figures 5(a)-(c) appear equivalent to induction vectors. We speculate that penetration depth of induction vectors and impedance(-derived) data differs at sites on the Gawler Craton. Moreover, induction vectors are dominated by the contrast between the conductive material at the edge of the craton and the (averaged) resistivity of the Gawler Craton. Lateral variations of conductivities within the craton at the depth of > 120 km, such as the alternating conductive and resistive bodies in Figs 5(a) and (b), are not resolved by induction vectors.

While inversion and forward modelling results point at the existence of strong conductivity contrasts in the depth range of 100-300 km which are oriented perpendicular to the average orientation of Φmax, lateral distance between conductive (appearing weakly in some results) and resistive units varies between each of the inversion results both shown here, and additional results obtained in this or the N22°W coordinate system. Assuming a single conductive body, as in Fig. 5a, inversion results would suggest that location of the body is only poorly constrained by the data so that it may appear at different locations with similar data fits.

However, high ellipticities and Φmax values may also point at the existence of electrical anisotropy (Heise *et al.* 2006, Löwer & Junge 2017). 3D inversion of ModEM is unable to model anisotropy but may fit the data in the presence of anisotropy by inserting alternating conductive and resistive structures. Similar behaviour was observed by Patro & Egbert (2011) in their inversion of profile data over the

Deccan Volcanic Province, Western India, and by Meqbel *et al.* (2014) in their inversion of long-period MT data over the north-western United States. The great variety of images of such alternating conductive and resistive features at depths > 120 km in Figs 5 could be related to differences in sensitivity to anisotropy between the data types and error settings used in the inversion. In the following a 3D conceptual model of the region is used to study these aspects.

4.2 Stage Ib: Conceptual models of the Gawler Craton

To test the resolution of structures > 100 km depth and compare sensitivities of various MT data types, we constructed a 3D conceptual model. To further reduce the level of structural details in the 3D model, we assigned a fixed value to resistivities of the original model within intervals (see Table 1). Resistivities ≥ 200 Ωm dominate at depths > 120 km in the conceptual base model and lower resistivities of 20 Ωm are only found at the southern edge of the survey area (lower panels in Fig. 7a).

Table 1:

Range (Ωm)	<1	1-5	5-100	100-500	500-5000	> 5000
Value (Ωm)	0.5	2	20	200	2000	5000

We created three model variants with different conceptual conductive structures at depths between 122 and 212 km (Fig. 7b-d) based on the modelling results of the previous section. In the first variant in Fig. 7(b), we introduce an azimuthally anisotropic body outlined by the craton boundaries with the resistive direction oriented N23°E, i.e., parallel to the long axis of phase tensor ellipses at long periods and the conductive direction perpendicular. Since ModEM does not permit intrinsic anisotropy, we simulated anisotropy by inserting a bundle of conductive lamellae along the *yz*-plane into the base model. Using Kirchhoff's law, bulk resistivities $\rho_{\parallel} = 2\rho_1\rho_2/(\rho_1 + \rho_2)$ and $\rho_{\perp} = (\rho_1 + \rho_2)/2$ parallel and perpendicular to the strike of the anisotropy can be calculated (e.g. Eisel & Haak 1999). With $\rho_1 = 3$ Ωm and $\rho_2 = 200$-2000 Ωm, effective bulk resistivities of the anisotropic structure yield $\rho_{\parallel} \approx 6$ Ωm and $\rho_{\perp} \approx$ 100-1000 Ωm, thus anisotropy ratios of 16-160. We also created two isotropic model variants: The second model variant contains a conductive block of 3 Ωm and dimensions of 175 km x 735 km, in the third model the entire base of the Gawler Craton is set to 3 Ωm.

4.2.1 Comparison of forward responses

Fig. 8 compares phase tensor responses of all three model variants for periods of 518 (upper panels) and 1389 s (lower panels); ellipse axes are normalised and colours show the value of Φmax..

Overall, the large-scale pattern of ellipse shapes and Φmax values has great similarities between all models. Outside the Gawler Craton, Φmax values < 45° (blue and green colours in Figs 8a-c) dominate and responses of the three variants are mostly similar. Comparison of responses to the response of the base model without any conductor shows that sensitivity to the base of the craton is mainly located at stations on the craton, whereas stations to the east and the west are nearly unaffected. In the latter region, thick sedimentary cover (1-3 km with resistivities < 10 Ωm) and the low resistivities at depths of 20 to 70 km along the craton edge attenuate EM signals much stronger. Hence, sensitivity to structures in the Gawler Craton at depths ≥ 120 km is limited to periods > 1000 s.

Yet, on the craton sedimentary cover is thin and resistivities range between 100 and 5000 Ωm. For a resistivity of 1000 Ωm, signals with a period of 60 s reach the top of the targets at 120 km depth. As a result, effects of the conductive structures can be seen in phase tensor data > 50 s, with the largest effects between 100 and 3000 s. In fact, responses of the three variants show distinct features at these sites. While Φmax values on the craton exceed 60° for all three variants, the spatial distribution differs for periods > 100 s. For the anisotropic model, Φmax values measure ~70° and are nearly constant over the entire craton (Fig. 8a). In contrast, both other responses show high Φmax values in the craton centre which decay towards the edges ranging between 70° and 50° for the block model (Fig. 8b) and 80° and 50° for the homogeneous variant (Fig. 8c). In addition, ellipticity of phase tensors decreases from left to right in Figure 8. For the anisotropic model, phase tensors have strong ellipticities and major axes on top of the craton are oriented parallel, pointing along the N23°E direction. For the block model, ellipticity is slightly lower and further decreases towards the western and eastern edges of the craton. For the homogeneous base, ellipses on the craton are overall more circular. Moreover, ellipses at the northern edge of the craton are aligned in east-west direction, different from the other variants where they are aligned with ellipses on the craton.

Figure 9 compares responses of induction vectors (Parkinson convention) of the three conceptual model variants. As for phase tensors, measurable influence of the conceptual conductors can mainly be seen at stations located on the craton and periods > 100 s. Responses for the anisotropic (Fig. 9a) and the single block variant (Fig. 9b) are quite similar. On top of the craton, induction vectors usually point radially away from the craton centre and differences are hard to be spotted visually. For the homogeneous conductive Gawler base, however, the radial pattern of induction arrows on the craton is significantly weaker (Fig. 9c).

Comparing the responses of the conceptual models to the observed data, we find that the conceptual model is in general able to explain the major features of the phase tensors (Fig. 1) and induction vectors (Fig. 2). Yet, for stations on top of the craton, only the anisotropic variant is able to reproduce both the constant and high Φmax values of about 70° across the entire craton as well as the high ellipticity. While a single conductive feature such as the block produces high Φmax values and ellipticities, it cannot explain the large spatial extent of constantly high Φmax values and ellipticities. We also tested various other lateral locations of the block within the Gawler Craton but results always showed a pronounced peak of Φmax values in the centre of the block, decaying towards its boundaries. Even more clearly, low ellipticities observed for a generally conductive craton base are inconsistent with the observations. Overall, the forward modelling tests with conceptual structures support the existence of electric anisotropy at the base of the Gawler Craton.

Finally, we test the hypothetical effect of the zone of electric anisotropy within the mantle on the responses at the station locations on the surface. This test aims to establish a measure of sensitivity as a function of period of various subsets of the data, e.g., impedance and phase tensor elements, to the presence of mantle anisotropy. For this purpose, we calculated data misfits between responses of the conceptual model variants and the base model in terms of normalised RMS (nRMS) errors, which we treat as a proxy for sensitivity (Fig. 10). The data errors are the same as for the field data inversions of section 4. Since the inversion scheme aims to minimise the data misfit, it is one of the driving forces of the inversion procedure. For phase tensor data, highest sensitivity (highest nRMS values) occurs for periods of 100-10,000 s with a maximum at ~700 s both for the uniform data error of 0.04 (Fig. 10a) and the combination of relative data errors of 4.24 % and a floor of 0.025 (Fig. 10b). Normalised RMS

values for constant errors are higher than for relative errors. In particular, sensitivity of the Φxx component is four (Fig. 10a) and two (Fig. 10b) times higher than for the other phase tensor components, respectively. In contrast, sensitivities/nRMS values of impedance components in Fig. 10(c) do not show a maximum within the inverted period range (dashed lines in Fig. 10a-c) but increase towards a maximum at longer periods. The impedance phase and, thus, the phase tensor, "anticipates" the magnitude response (dispersion relation, Weidelt 1973) and sensitivity of phases occurs at shorter periods than that of real and imaginary parts or magnitudes (apparent resistivities).

Differences in absolute nRMS levels and distribution with period may be related to structural differences at depths > 100 km in resistivity models of the field data described in section 4 (Fig. 5). For phase tensors and uniform data errors, for which sensitivity to the anisotropy is highest, conductive bodies between 120 and 300 km depth are most pronounced. Accordingly, weakest conductors occurred for inversion of impedances which appear less sensitive to anisotropic conductors at the base of the Gawler Craton. Higher normalised RMS values / sensitivities for impedances could be generated by reducing data errors. In practice, errors chosen here are low (cf. section 4) and using lower errors resulted in poorer convergence of 3D inversion.

Conductivity contrasts affect particularly the phase relationship of impedances which can be seen as a clear peak of sensitivity for phase tensors in Figures 10(a)-(b). Considering impedances as real and imaginary parts, as in impedance inversion, sensitivity is shifted towards higher periods and distributed over a wider period range which extends beyond the maximum period of 13,000 s considered here. In inversion, data were used only for periods up to 3730 s. Increasing the period range for impedance data may improve recovery of deep conductive material. Yet, measurements at longer periods within several hundreds of km (depending on geometry and resistivities) of coastlines may not be consistent with modelling in Cartesian coordinates but require a spherical approach (Grayver *et al.* 2019) and will therefore not be considered here.

4.2.2 Inversion tests

We also performed inversion tests with the anisotropic variant of the conceptual model. Prior to inversion, Gaussian noise was added to the data according to the data error settings. Inversion parameters

for data and model were the same as for the field data (cf. section 3). Resolution of structures < 100 km is excellent and very similar for all data types. Hence, Figure 11 shows horizontal slices of the resistivity models only for depths between 120 and 300 km.

Overall, resistivity models of the conceptual craton base in Figures 11(a)-(c) look quite similar. Low resistivities of the anisotropic body are imaged as three (Figs 11a-b) or two (Fig. 11c) subparallel conductive (< 20 Ωm) bodies aligned with the conductive anisotropy direction within a resistive (~1000 Ωm) background.

Location of the anomalies appears at the same position for all data types. The largest body extends ~700 km across the entire width of the Gawler Craton and is located ~50 km north of the coastline. The second body common to all bodies is located at the northern edge of the craton and measures 200 km along-strike. Phase tensor inversion results additionally show a conductive feature located partly offshore at the southern tip of the Eyre Peninsula. Also, conductance of the anomalous bodies and resistivity contrasts are higher for the phase tensor results than for the impedance model.

Final RMS values (1.27, 1.26, 1.42) are at comparable levels for all three inversions and model responses appear similar when plotted as phase tensors (Figs 12a-c). Closer inspection of phase tensor properties Φmax, Φmin and Φmax- Φmin (Figs 12d-f) reveal a systematic underfitting of Φmax values and, thus, the phase difference Φmax- Φmin, by up to -10° for the highest Φmax values of the impedance inversion result; for phase tensors inversions these parameters are usually fit within ±3°.

Intensity of conductivity contrasts and systematic misfits of phase tensor properties, similar correlations with inverted data type, and data error settings as for the field data sets (cf. Figs 5-6) further support the hypothesis of electric anisotropy at the base of the Gawler Craton. Differences in inversion models of the conceptual data set are less pronounced than in the field examples. We speculate that this may be result of a combination of simpler overall structure in the conceptual data (not including unrecovered structural details of the original data set), lower anisotropy ratio, lower and controlled noise levels and absence of distortion in impedance data for the conceptual data set.

5 STAGE II: 3D INVERSION OF THE GAWLER FIELD DATA SET WITH A PRIORI INFORMATION ON ANISOTROPY

Finally, we added a priori information on anisotropy based on the results of the forward modelling studies to inversions of the field data. We used the 1D layered model of section 3.1 but now added lamellae of 3 Ωm to the 1D model between 120-210 km depth within the Gawler Craton, i.e. at the same positions as in the conceptual model (cf. Fig. 7b), and otherwise kept the resistivities of the 1D layered model (~270 Ωm). The setup corresponds to anisotropic resistivities of $\rho_{\parallel} \approx 6$ Ωm and $\rho_{\perp} \approx 140$ Ωm and an anisotropy ratio of 23. All other inversion parameters were the same as before. In particular, a priori resistivities of the model were allowed to change during inversion.

Based on the results of Fig. 5, we used phase tensors with constant errors (Fig. 13a) and impedances (Fig. 13b), both jointly with induction vectors. In the upper 60 km, inversion models are nearly identical to results of Figs 5(a) and (c). At depths > 60 km, the new inversions differ from previous models, but interestingly phase tensor and impedance results are much more consistent. Directly above (70-120 km) and below (> 212 km) the anisotropic body, both of the new inversion models show quite uniform structures with resistivities usually between 200 and 5000 Ωm. Different from results in Figs 5(a) and (c), significantly less conductive bodies along the craton edge persist beyond 70 km depth. Similarly, extended conductive bodies with resistivities < 20 Ωm at depths > 212 km are absent. At depths of the anisotropy, resistivities are increased from the starting model in both inversion results. Inversion of phase tensors adds low resistivities at the south-eastern margin of the Gawler Craton.

Normalised RMS misfits of 4.02 (Fig. 13a) and 4.67 (Fig. 13b) are reduced by 0.13 and 0.10, respectively, from the initial inversions using the 1D layered half space. For both inversions, induction vectors are fitted equally well as in the initial inversion, where reduction of misfit is largest for phase tensors (-0.25) and impedances (-0.15) and within a period range of 200 to 1500 s. In particular, fits of phase tensor parameter Φmax and the phase difference Φmax-Φmin are improved by ~5° for large values (Fig. 14).

Model regularisation only allows variations from the prior (=starting) model which are smooth over several neighbouring cells. Hence, the contrast between the conductive lamellae and the background

resistivity, which determines the anisotropy ratio, cannot be modified by the inversion process. Since previous inversions suggested higher resistivities at depths > 120 km and stronger contrasts, we increased resistivities of the 1D starting model at depth >120 km to 1000 Ωm and subsequently anisotropic lamellae of 3 Ωm were added. The new model has anisotropic resistivities of $\rho_{\parallel} \approx 6$ Ωm and $\rho_{\perp} \approx 500$ Ωm and an anisotropy ratio of 83.

Inversion models for the same data sets as before are shown in Figs 13(c) and (d). As before, results in the upper 60 km are very similar to the models using the isotropic starting model. At depths of 70-120 km and > 212 km resistivity structures are again more uniform than in results of Fig. 5 but show a few conductive bodies to the east and the west of the Gawler Craton which were not present in Figs 13(a) and (b). In between the anisotropic zone, resistivities are increased in the centre of the Gawler Craton compared to the starting model.

Inversions for both phase tensors/tipper and impedances/tipper yield even lower misfits than previous results of Figs 13(a, b) and Figs 5(a, c). Normalised RMS values are 3.81 (-0.34 compared to result of Fig. 5(a)) and 4.45 (-0.33 w.r.t Fig. 5(c)) for the models in Figs 13(c) and (d), respectively. In particular for the impedance/tipper inversion, phase tensor parameters Φmax, Φmin and Φmax-Φmin are recovered more reliably (Fig. 14).

Figure 13 shows that the presence of anisotropy at the base of the Gawler Craton at depths of 120-212 km reduces the complexity of resistivity structures at depths > 70 km compared to an isotropic starting model. Outside the anisotropic region, resistivities are almost uniform laterally. While alternating conductive and resistive bodies extended from 70 to > 300 km depth for the isotropic starting model in the mantle, the anisotropic zone is limited to a depth interval of ~90 km for the model with an anisotropic prior. We would also like to point out that structures revealed by phase tensor and impedance inversions are very similar. In combination, results of Figures 13 and 14 illustrate that presence of electric anisotropy of the Gawler Craton not only is compatible with the field data set but leads to more consistent modelling results and improves data fit.

6 DISCUSSION AND RESULTS

Overall, 3D inversion can explain large parts of the Gawler data set with an isotropic resistivity structure. Structures from surface to ~70 km depth are imaged similarly for both phase tensor and impedance inversion as well as for a wide variety of inversion parameters. Sedimentary basins in the upper 2.5 km were imaged consistently and conductive bodies > 10 km in extent along the onshore edge of the Gawler Craton, the Stuart Shelf and the Flinders Ranges were mapped at the same positions.

However, isotropic inversions failed to produce a unifying model and fit the data set to a similar level at depths > 70 km. Rather, inversion results point at the existence of anisotropy at depths > 100 km: All models showed alternating conductive and resistive structures of variable widths at depths of 120–300 km trending ~N60°W/S30°E, which may be understood as an attempt of the isotropic inversion to model anisotropy. Similar behaviour was observed in field data inversions (e.g. Patro & Egbert 2011, Meqbel *et al.* 2014, Bedrosian *et al.* 2019, Kirkby & Duan 2019) and synthetic studies (e.g. Löwer & Junge 2017).

Another indication of anisotropy is the behaviour of phase tenors at sites located on the Gawler Craton and periods > 300 s. Here, high Φmax values and ellipticities (~Φmax-Φmin) as well as wide-reaching alignment of Φmax directions parallel to ~N23°E can be observed. In a modelling study, Löwer & Junge (2017) showed that above anisotropic structures major axes align perpendicular to the conductive direction of an azimuthally anisotropic body (see also Heise *et al.* 2006) and ellipticity increases with the anisotropy contrast.

For the Gawler data set, we could finally obtain a unifying model for all data types when inserting an anisotropic body at the base of the Gawler Craton into the prior/starting model with the conductive direction perpendicular to the median direction of phase tensor major axes (N23°E).

Presence of anisotropy at the base of the Gawler Craton reduced the complexity of resistivity structures at depths > 70 km compared to an isotropic starting model. Outside the anisotropic region, resistivities are laterally nearly uniform. While alternating conductive and resistive bodies extended from 70 to > 300 km depth, the anisotropic zone is limited to a depth interval of ~90 km. We would also like to point out that structures revealed by phase tensor and impedance inversions are very similar. Moreover,

normalised RMS values improved by 0.1 to 0.34 compared to inversions with isotropic starting models. The results illustrate that presence of electric anisotropy of the Gawler Craton not only is compatible with the field data set but leads to more consistent modelling results and improves data fit.

Induction vectors of this data have poor sensitivity to the base of the Gawler Craton and corresponding data fits were similar for all inversions and not affected by a priori information on anisotropy.

Forward modelling and inversion tests with a conceptual model and both isotropic and anisotropic variants of conductors at the base of the Gawler Craton support the existence of anisotropy. With isotropic variants, long period data on the Gawler Craton could not be explained. Also, inversion tests contained alternating elongated conductive and resistive bodies to account for anisotropy in the data. Analogous to the field inversions, replacement structures extend to shallower and deeper depths (70-300 km) than the true anisotropic structure (120-212 km). Differences in inversion outcomes between data types and phase tensor error settings were less pronounced. We speculate that this is due to the lower complexity and conductivity contrasts of the conceptual model.

We would like to add that anisotropic structures shown for the Gawler Craton contain purely azimuthal anisotropy, which is well defined by the directions of the major axes of the phase tensors. Because of horizontal current systems, MT data are mainly sensitive to the horizontal projection of anisotropy (Heise *et al.* 2006). Thus, anisotropy dip and slant angles (e.g. Martí 2014) are often poorly resolved and there is no reason to assume non-zero values for these angles for the Gawler region.

We simulated about 100 alternatives varying lateral extent, thickness, depth location and anisotropy ratio, included in the conceptual model as wells as in selected field inversion results. Fig. 15 illustrates our preferred variant with respect to location and extent which best explains the measured data. The top of the anisotropic zone coincides with the mid-lithospheric discontinuity (MLD) proposed by Skirrow *et al.* (2018) (Fig. 15b). The authors define the MLD as the lower boundary of a region of low-Vp/Vsh at about 130 km below surface stretching through large parts of the Gawler Craton. Skirrow *et al.* (2018) infer that the MLD separates an upper, dominantly depleted lithospheric mantle from a lower, predominantly fertile one. We propose that the anisotropic zone extends through the deeper, fertile

lithospheric mantle down to the lithosphere-asthenosphere boundary at 200 (Kennett *et al.* 2013) to 250 km (Czarnota *et al.* 2014) depth.

While the MT data set does not provide strong limitations on a maximum thickness of the zone, we preclude continuation of this anisotropic zone into the asthenosphere. Currently, the Australian Plate is moving towards NNE at a speed of > 7 cm/yr (DeMets *et al.* 1990) and, if present, electric anisotropy in the asthenospheric mantle would be expected to feature the conductive direction SSW-NNE parallel to the mantle flow. (e.g. Bahr & Simpson 2002, Gatzemeier & Tommasi 2006, González-Castillo *et al.* 2019). Such alignment would be different from the suggested orientation by 90 degree and is inconsistent with the data. The lateral extent of the anisotropic body is less well constrained. On the Gawler Craton, thin (~200 m) sedimentary cover and high resistivities (mostly > 1000 Ωm) provide a window for MT signals to penetrate to the deep lithosphere. However, at its edges, conductive material strongly attenuates the electromagnetic fields and resolution at depths > 100 km is significantly poorer. Our modelling results suggest that the anisotropic body stretches at least throughout the resistive window on land. The data would be consistent with an extent to ~100 km beyond the craton boundaries, but we can exclude persistence throughout the entire survey region and beyond within a layer at constant depth. Our suggested body follows the geologic boundary of the Gawler Craton (Korsch & Doublier 2015), but prevalence limited to the southern part (cf. Figs 15a-b) may be similarly reasonable based on its proposed genesis, which is discussed in the following.

The data set had been previously modelled and interpreted by Thiel & Heinson (2013) and Thiel *et al.* (subm.). The 3D conductivity models of these studies suggest the presence of a single conductive body at depths of 70 to 200 km similar to the results shown in Fig. 5(a). As discussed above, such a conductivity distribution is in good agreement with impedances and induction vectors inverted for the results in Fig. 5(a), Thiel & Heinson (2013) and Thiel *et al.* (subm.) and does explain these data types similarly well. Based on the results for inversion of phase tensors and detailed analysis of the fit of phase tensors, however, we prefer the anisotropic model over the isotropic one since it explains all representations of the MT impedance similarly well. The findings are consistent with the geological genesis of the elevated conductivities in the anisotropic region suggested by previous studies, but point

at an anisotropic manifestation of electrically conductive mineral phases in the lower lithospheric mantle.

For the survey area, several studies based on SKS and shear-wave splitting (Simons *et al.* 2002) and isostatic uplift (Simons *et al.* 2003, Kirby *et al.* 2006) showed azimuthal seismic anisotropy with fast directions aligned ENE-WSW, which is in good agreement with the conductive direction of our anisotropic zone. These studies suggest presence of seismic anisotropy between 80 and 200 km, but vertical resolution of SKS analysis is rather poor, caused by the use of seismic waves with near-vertical ray paths and long wavelengths for analysis. In contrast, MT data resolve upper boundaries of conductors, including anisotropic zones, particularly well.

Azimuthal (seismic) anisotropy of the upper mantle is generally interpreted as a consequence of the strain-induced crystallographic texture or lattice preferred orientation of intrinsically anisotropic mantle minerals, principally olivine (Silver, 1996; Savage, 1999). Such "frozen" deformation can be vertically coherent over wide parts of the lithosphere (Silver 1996). For olivine, the [100] axis (= fast direction) aligns perpendicular to the (mechanically weak) direction which accumulates the shortening. As a result, maximum propagation speed is parallel to structural trends and perpendicular to compression.

For the anisotropic body in our resistivity models, resistivities of 100 to 1000 Ωm modelled for the resistive direction are within the range of laboratory measurements for olivine under lithospheric conditions and depths of 100-200 km (Pommier 2014). Anisotropy ratios of our forward and inversion models shown in sections 4.2 and 5 range between 16 and 160. Overall, fit of data sensitive to the anisotropic body improved with increasing anisotropy ratio. In view of the entire bundle of alternative modelling results, we conclude that a minimum ratio of 30, corresponding to resistivities of 3 to 30 Ωm along the conductive direction, is required to explain the data. Considering results of laboratory measurement, this anisotropy ratio is difficult to explain based on properties of olivine alone.

For the Gawler Craton, presence of melt fractions which could lower resistivities parallel to aligned crystals and, thus, increase anisotropy can be excluded. We suggest that the overall anisotropy of the deep Gawler Craton could result from a combination of lattice preferred oriented olivine and overprinting by macroscopic anisotropy. One geodynamic model developed by Skirrow *et al.* (2018)

suggests that the survey region was subject to subduction between ~1.7 and 1.5 Ga (see Fig. 15b). Associated water release of the subducting slab induced metasomatic processes and refertilization of the lithospheric mantle, in particular in the southern part of the Gawler Craton. Skirrow *et al.* (2018) interpret a low resistive body imaged in the lower lithospheric mantle by Thiel & Heinson (2013) as local accumulation of water in the form of water-bearing minerals and associated metamorphic products.

Based on the new modelling results, we speculate that the compressional stress field caused by the collision of the Gawler Craton and the oceanic collider and the subsequent extension resulted in preferential orientation of weakness perpendicular to the compressional direction. As a result, rise of water from the subducting slab and associated metamorphic processes are thought to have occurred primarily along these weakened zones, thus resulting in (macroscopic) electric anisotropy. In our modelling study, anisotropy was only required to be present beyond depth of 70 to 100 km, which suggests that metamorphic processes which led to the presence of conductive phases mainly occurred beneath the MLD. We would also like to point out that anisotropy ratios in the modelling study were constant over the entire zone of anisotropy. In reality, anisotropy ratios may vary in the zone. We speculate that water release and concentration of conductive mineral phases may be highest where Thiel & Heinson (2013) imaged the conductive body and levels out towards the edges of the proposed anisotropic body. More detailed investigation of anisotropy, however, is beyond the scope of the data set and this work.

7 CONCLUSIONS

Direct measurements of electrical anisotropy of the sub-continental lithospheric mantle are difficult to prove given the receding sensitivity of magnetotelluric data with depth, three-dimensional effects caused by both lateral and vertical conductivity structure and lack of distinct MT data properties which singularly attest to anisotropy. We have shown that magnetotelluric phase tensor data can provide valuable information for identification and characterization of electric anisotropy of the subsurface which may be otherwise missed with interpretation of MT impedances only.

Our analyses of the Gawler data and complementary synthetic data sets illustrate that a combination of high phase tensor maximum phase (phimax) values, high ellipticities and aligned major axes which persist over a large area is suggestive of anisotropic features. If caused by a single anisotropic feature, orientation of phase tensor axes provides a first order estimate of the horizontal projection of resistive/conductive direction. In our modelling study, inversion of phase tensors resulted in pronounced conductivity contrasts at corresponding depths, when using constant errors. In contrast, impedance data were equivalently fit with a single, isotropic conductive body found at the same depth but with much smaller extent along the resistive axis of the anisotropy. Overall, it was only possible to find a model which explains both impedances and phase tensors (as well as induction vectors) because we inspected data fits and model structures of a series of inversion results in detail and finally "merged" resistivity structures manually into a unifying model.

Based on the analysis of the Gawler data and our modelling studies, we propose the presence of electric anisotropy for the lower lithosphere of the Gawler Craton beneath the MLD (>120 km). Orientation and depth extent correlate spatially with seismic anisotropy inferred from studies on shear-wave splitting and isostatic uplift. We suggest that the electric anisotropy is a result of a combination of lattice-preferred orientation of olivine crystals and macroscopic overprinting of metamorphic processes related to Proterozoic subduction (Skirrow *et al.* 2018; Tiddy & Giles 2020).

Like the Gawler Craton, 3D resistivity models of the lithospheric mantle of south-eastern Australia (Kirkby *et al.* 2020) and the Musgrave Province (Thiel *et al.* 2020) show similar patterns of alternating resistive and conductive mantle. Given the insights presented here, we suggest that electrical anisotropy, at least of part of the Australian lithospheric mantle, is present and should be accounted for in geodynamic and tectonic interpretations. More generally, we recommend testing for anisotropy if any of the features, and particularly if several of those described here, are found in a data set or model.

The overarching goal of inversion and subsequent interpretation of the inversion results is obtaining a unifying model which is able to explain all aspects of the data set. To achieve this, we advocate to perform a series of inversions of various data types, both separately and jointly. Since each data type entails a specific sensitivity to underground structures, inversion of various data types may reveal different features of the subsurface particularly well (or poorly). Though describing the same

underground structure, these models will inherently look different, but should be considered as complementing images. Thus, a unifying model which explains all aspects of a data set to the same degree is not likely to be found by picking a single best model by a single criterion, such as the one with the "overall lowest misfit". Rather, establishing a comprehensive model of the electrical resistivity distribution is likely to involve more efforts by the modeller to "merge" features of the range of models in order to obtain a single "best" model.

APPENDIX

A1 – Decomposition of the phase tensor

The phase relation of the impedance tensor can be expressed by the phase tensor (Caldwell *et al.* 2014)

$$\Phi = \mathbf{X}^{-1}\mathbf{Y},$$

where X and Y are the real and imaginary part of the magnetotelluric impedance $\mathbf{Z} = \mathbf{X} + i\mathbf{Y}$. Φ

$$\Phi = \begin{pmatrix} \Phi_{xx} & \Phi_{xy} \\ \Phi_{yx} & \Phi_{yy} \end{pmatrix}$$

is a real, second rank tensor and is characterized by a direction and three independent scalar coordinate invariants. Caldwell *et al.* (2004) suggest to use maximum (Φ_{max}) and minimum (Φ_{min}) tensor values and the tensor skew (β)

$$\beta = \frac{1}{2}\tan^{-1}\left(\frac{\Phi_{xy} - \Phi_{yx}}{\Phi_{xx} + \Phi_{yy}}\right)$$

as coordinate invariants. Using this notation, the phase tensor can be rewritten as

$$\Phi = \mathbf{R}^T(\alpha - \beta)\begin{pmatrix} \Phi_{max} & 0 \\ 0 & \Phi_{min} \end{pmatrix}\mathbf{R}^T(\alpha + \beta)$$

where $\mathbf{R}(\alpha + \beta)$ is the rotation matrix

$$\mathbf{R}(\alpha + \beta) = \begin{pmatrix} \cos(\alpha + \beta) & \sin(\alpha + \beta) \\ -\sin(\alpha + \beta) & \cos(\alpha + \beta) \end{pmatrix}$$

and

$$\alpha = \frac{1}{2}\tan^{-1}\left(\frac{\Phi_{xy} + \Phi_{yx}}{\Phi_{xx} - \Phi_{yy}}\right)$$

expresses the dependence of the phase tensor on the coordinate system.

8 ACKNOWLEDGEMENTS

South Australian AusLAMP data used in modelling were funded by initiatives of the Department for Energy and Mining. Logistical support was provided by Geoscience Australia for some of the acquisition. Co-funding was provided by Geoscience Australia for 50 sites. Funding for the Musgrave MT sites was provided by NCRIS. Data were processed to EDI format using Bounded influence robust remote referencing (BIRRP; Chave 1989). This work was supported by computational resources at Helmholtz Centre Potsdam – GFZ German Research Centre for Geosciences and those provided by the Australian Government through the University of Adelaide under the National Computational Merit Allocation Scheme. We thank Traditional Owners and landholders for granting access to their land. Thank you to AuScope for providing access to their instrumentation pool, and to Goran Boren for maintaining these instruments. Kristina Tietze was funded by postdoctoral research scholarship of the German Academic Exchange Service (DAAD).

9 REFERENCES

Amante, C. & Eakins. B.W., 2009. ETOPO1 1 Arc-Minute Global Relief Model: Procedures, Data Sources and Analysis. NOAA Technical Memorandum NESDIS NGDC-24. National Geophysical Data Center, NOAA, August 2018. doi:10.7289/V5C8276M.

Bahr, K. & Simpson, F., 2002. Electrical anisotropy below slow-and fast-moving plates: paleoflow in the upper mantle? *Science*, **295**(5558), 1270–1272.

Bedrosian, P. A., Peacock, J. R., Dhary, M., Sharif, A., Feucht, D. W. & Zahran, H., 2019. Crustal magmatism and anisotropy beneath the Arabian Shield —A cautionary tale. *Journal of Geophysical Research: Solid Earth*, 124. https://doi.org/10.1029/2019JB017903

Booker, J., 2013. The Magnetotelluric Phase Tensor: A Critical Review, *Surv. Geophys.*, **35**(1), 7—40.

Caldwell T.G., Bibby H.M. & Brown C. 2004. The magnetotelluric phase tensor, *Geophys. J. Int.*, **158**, 457—469.

Cao, H., Wang, K., Wang, T. & Hua, B., 2018. Three-dimensional magnetotelluric axial anisotropic forward modeling and inversion. *Journal of Applied Geophysics*, **153**, 75-89. https://doi.org/10.1016/j.jappgeo.2018.04.015.

Chave, A.D. & Thomson, D.J., 2004. Bounded influence magnetotelluric response function estimation. *Geophys J Int*, **157**, 988–1006, doi: 10.1111/j.1365-246X.2004.02203.x.

Curtis, S. & Thiel, S. 2019. Identifying lithospheric boundaries using magnetotellurics and Nd isotope geochemistry: An example from the Gawler Craton, Australia. *Precambrian Research*, **320**, 403 – 423.

Czarnota, K., Roberts, G.G., White N.J. & Fishwick, S. 2014. Spatial and temporal patterns of Australian dynamic topography from River Profile Modeling. *J. Geophys. Res. Solid Earth*, **119**, 1384–1424, doi:10.1002/2013JB010436.

Dai, L. & Karato, S. 2009. Electrical conductivity of orthopyroxene: Implications for the water content of the asthenosphere. *Proc. Jpn. Acad.*, Ser. B, **85**, 466–475, doi:10.2183/pjab.85.466.

DeMets, C., Gordon, R:G., Argus, D.F. & Stein, S., 1990. Current plate motions. *Geophys J Int*, **101**, 425—478.

Eaton, D.W., Jones, A.G. & Ferguson I.J., 2004. Lithospheric anisotropy structure inferred from collocated teleseismic and magnetotelluric observations: Great Slave Lake shear zone, northern Canada. *Solid Earth*, **31**(19), L19614.

Egbert, G.D. & Kelbert, A., 2012. Computational recipes for electromagnetic inverse problems. *Geophys. J. Int.*, **189**, 251–267.

Eisel M. & Haak V., 1999. Macro-anisotropy of the electrical conductivity of the crust: a magnetotelluric study of the German Continental Deep Drilling site (KTB). *Geophys. J. Int.,* **136**, 109–122.

Fraser, G., McAvaney, S., Neumann, N., Szpunar, M. & Reid, A., 2010. Discovery of early Mesoarchean crust in the eastern Gawler Craton, South Australia. *Precambrian Research*, **179**(1-4), 1-21

Gardés, E., Gaillard, F. & Tarits, P., 2014. Toward a unified hydrous olivine electrical conductivity law. *Geochemistry, Geophysics, Geosystems*, **15**, 4984-5000.

Gatzemeier, A. & Moorkamp M., 2005. 3D modelling of electrical anisotropy from electromagnetic array data: hypothesis testing for different upper mantle conduction mechanisms. *Physics of the Earth and Planetary Interiors*, **149**, 225–242.

Gatzemeier, A. & Tommasi, A., 2005. Flow and electrical anisotropy in the upper mantle: Finite-element models constraints on the effects of olivine crystal preferred orientation and microstructure. *Physics of the Earth and Planetary Interiors*, **158**(2–4), 92—106.

González-Castillo, L., Bohoyo, F., Junge, A., Galindo-Zaldívar, J., Cembrowski, M., Torres-Carbonell, P., Ruiz-Constán, A. Pedrera, A., Ibarra, P., Maestro, A. & Ruano, P., 2019. Mantle flow and deep electrical anisotropy in a main gateway: MT study in Tierra del Fuego. *Scientific Reports*, **9,** 7148. https://doi.org/10.1038/s41598-019-43763-w.

Grayver, A.V., van Driel, M. & Kuvshinov, A.V., 2019. Three-dimensional magnetotelluric modelling in spherical Earth. *Geophysical Journal International*, **217**(1), 532–557, https://doi.org/10.1093/gji/ggz030.

Guo, Z., Egbert, G., Dong, H. & Wei, W. 2020. Modular finite volume approach for 3D magnetotelluric modeling of the Earth medium with general anisotropy. *Physics of the Earth and Planetary Interiors*. **309**, 106585, https://doi.org/10.1016/j.pepi.2020.106585.

Hand, M., Reid, A. & Jagodzinksi, L., 2007. Tectonic Framework and Evolution of the Gawler Craton, Southern Australia, *Economic Geology*, **102**, 1377–1395.

Häuserer, M. & Junge, A. 2011. Electrical mantle anisotropy and crustal conductor: a 3-D conductivity model of the Rwenzori Region in western Uganda. *Geophysical Journal International*, **185**, 1235-1242.

Heise, W., Caldwell, T., Bibby, H. & Brown, C. 2006. Anisotropy and phase splits in magnetotellurics. *Physics of the Earth and Planetary Interiors*, **158**(2), 107–121.

Heinson, G., Didana, Y., Soeffky, P., Thiel, S. & Wise, T., 2018. The crustal geophysical signature of a world-class magmatic mineral system. *Sci Rep*, **8,** 10608. https://doi.org/10.1038/s41598-018-29016-2

Heinson, G., Kay, B., Loader, L., Robertson, K. & Thiel, S., 2022. A global magnetotelluric graphite type locality: Multi-decade, multi-scale studies of the Eyre Peninsula anomaly. *Gondwana Research*, **105**, 388-398. https://doi.org/10.1016/j.gr.2021.09.017

Kelbert, A., Meqbel, N., Egbert, G.D. & Tandon, K., 2014. ModEM: A modular system for inversion of electromagnetic geophysical data. *Computers & Geosciences*, **66**, 40–53.

Kennett, B.L.N., Fichtner, A., Fishwick, S. & Yoshizawa, K., 2013. Australian Seismological Reference Model (AuSREM): mantle component. *Geophysical Journal International*, **192**, 871-887.

Kirkby, A. & Duan, J. 2019. Crustal structure of the eastern Arunta region, Central Australia, from magnetotelluric, seismic, and magnetic data. *Journal of Geophysical Research: Solid Earth*, **124**, 9395–9414.

Kirkby, A.L., Musgrave, R.J., Czarnota, K., Doublier, M.P., Duan, J., Cayley, R.A. & Kyi, D. 2020. Lithospheric architecture of a Phanerozoic orogen from magnetotellurics: AusLAMP in the Tasmanides, southeast Australia. *Tectonophysics*, **793**, 228560.

Korsch, R.J. & Doublier, M.P., 2015. Major crustal boundaries of Australia. Geoscience Australia.dataset. http://pid.geoscience.gov.au/dataset/ga/83223.

Le Pape, F., Jones, A.G., Vozar, J. & Wenbo, W. 2012. Penetration of crustal melt beyond the Kunlun Fault into northern Tibet. *Nature Geoscience*, **5**, 330-335.

Liu, Y., Junge, A., Yang, B., Löwer, A., Cembrowski, M. & Xu, Y. 2019. Electrically anisotropic crust from three-dimensional magnetotelluric modeling in the Western Junggar, NW China. *Journal of Geophysical Research: Solid Earth*, **124**. https://doi.org/10.1029/2019JB017605

Löwer A. & Junge A., 2017. Magnetotelluric Transfer Functions: Phase Tensor and Tipper Vector above a Simple Anisotropic Three-Dimensional Conductivity Anomaly and Implications for 3D Isotropic Inversion. *Pure Appl. Geophys*., **174** (2017), 2089–2101.

Martí, A. 2014. The Role of Electrical Anisotropy in Magnetotelluric Responses: From Modelling and Dimensionality Analysis to Inversion and Interpretation. *Surv Geophys*, **35**, 179-218.

Meqbel, N., Egbert, G.D., Wannamaker, P.E., Kelbert, A. & Schultz, A. 2014. Deep electrical resistivity structure of the northwestern U.S. derived from 3-D inversion of USArray magnetotelluric data. *Earth and Planetary Science Letters*, **402**, 290–304.

Miensopust, M.P. 2017. Application of 3-D Electromagnetic Inversion in Practice: Challenges, Pitfalls and Solution Approaches. *Surv Geophys*, **38**, 869–933, https://doi.org/10.1007/s10712-017-9435-1.

Murphy, B.S. & Egbert, G.D., 2017. Electrical conductivity structure of southeastern North America: Implications for lithospheric architecture and Appalachian topographic rejuvenation. *Earth and Planetary Science Letters*, **462**, 66-75.

NOAA National Geophysical Data Center 2009: ETOPO1 1 Arc-Minute Global Relief Model. NOAA National Centers for Environmental Information. Accessed August 2018.

Padilha, A.L., Vitorello, I., Pádua, M.B. & Bologna, M.S., 2006. Deep anisotropy beneath central-southeastern Brazil constrained by long period magnetotelluric data. *Phys. Earth Planet. Int*., **158**, 190–209.

Patro, P.K. & Egbert, G.D. 2011. Application of 3D inversion to magnetotelluric profile data from the Deccan Volcanic Province of Western India. *Physics of the Earth and Planetary Interiors*, **187**(1), 33–46.

Patro, P.K., Uyeshima, M. & Siripunvaraporn, W., 2013. Three-dimensional inversion of magnetotelluric phase tensor data. *Geophysical Journal International*, **192**(1), 58-66.

Pawley M.J., Dutch, R.A., Nestola, F. & Smyth, J.R., 2020. The relationship between crustal architecture, deformation, and magmatism in the Coompana Province, Australia. *Tectonics*, **39**(12), https://doi.org/10.1029/2019TC005593.

Poe, B.T., Romano, C., Nestola, F. & Smyth, J.R., 2010. Electrical conductivity anisotropy of dry and hydrous olivine at 8 GPa. *Physics of the Earth and Planetary Interiors*, **181**, 103-111.

Pommier, A., 2014. Interpretation of Magnetotelluric Results Using Laboratory Measurements. *Surveys in Geophysics*, **35**, 41-84. DOI 10.1007/s10712-013-9226-2.

Pommier, A., Kohlstedt, D.L., Hansen, L.N., Mackwell, S., Tasaka, M., Heidelbach, F. & Leinenweber, K. 2018. Transport properties of olivine grain boundaries from electrical conductivity experiments. *Contributions to Mineralogy and Petrology*, **173**(41).

Reid, A.J., Jagodzinski, E.A., Wade, C.E., Payne, J.L., Jourdan F., 2017. Recognition of c. 1780 Ma magmatism and metamorphism in the buried northeastern Gawler Craton: Correlations with events of the Aileron Province. *Precambrian Research*, **302**, 198-220.

Reid, A. 2019. The Olympic Cu-Au Province, Gawler Craton: a review of the lithospheric architecture, geodynamic setting, alteration systems, cover successions and prospectivity. *Minerals*, **9**(6), 371, doi:10.3390/min9060371.

Reid, A.J. & Hand, M., 2012. Mesoarchean to mesoproterozoic evolution of the southern Gawler Craton, South Australia. *Episodes*, **35**(1), 216-225.

Robertson, K., Thiel, S. & Meqbel, N., 2020. Quality over quantity: on workflow and model space exploration of 3D inversion of MT data. *Earth Planets Space*, **72,** 2. https://doi.org/10.1186/s40623-019-1125-4.

Samrock, F., Grayver, A.V., Eysteinsson, H. & Saar, M., 2018. Magnetotelluric image of transcrustal magmatic system beneath the Tulu Moye geothermal prospect in the Ethiopian Rift. *Geophysical Research Letters*, **45**, 12,847–12,855. https://doi.org/10.1029/2018GL080333.

Savage, M.K., 1999. Seismic anisotropy and mantle deformation: what have we learned from shear wave splitting? *Rev. Geophys*. **37**, 65–106.

Silver, P.G., 1996. Seismic anisotropy beneath the continents: Probing the Depths of Geology. *Annual Review of Earth and Planetary Sciences*, **24**, 385-432. https://doi.org/10.1146/annurev.earth.24.1.385

Skirrow, R.G., van der Wielen, S.E., Champion, D.C., Czarnota, K. & Thiel, S., 2018. Lithospheric architecture and mantle metasomatism linked to iron oxide Cu-Au ore formation: Multidisciplinary evidence from the Olympic Dam region, South Australia. *Geochemistry, Geophysics, Geosystems*, **19**, 2673–2705. https://doi.org/10.1029/2018GC007561

Smith, W. & Sandwell, D., 1997. Global sea floor topography from satellite altimetry and ship depth soundings. *Science*, **277**(5334), 1956–1962.

Swain, G., Woodhouse, A., Hand, M, Barovich, K., Schwarz, M. & Fanning, C.M., 2005. Provenance and tectonic development of the late Archaean Gawler Craton, Australia; U–Pb zircon, geochemical and Sm–Nd isotopic implications. *Precambrian Research*, **141**(3–4), 106-136.

Thiel, S., Goleby, B.R., Pawley, M.J. & Heinson, G., 2020. AusLAMP 3D MT imaging of an intracontinental deformation zone, Musgrave Province, Central Australia. *Earth, Planets and Space*, **72**, 98.

Thiel, S., Reid, A., Heinson, G. & Robertson, K., 2018. Mapping and characterizing lithosphere discontinuities: examples of southern Australia using AusLAMP MT. *Proceedings of the 24th Electromagnetic Induction Workshop, Helsingor, Denmark*, 2018.

Thiel, S. & Heinson, G., 2009. Regional MT survey across an Archaean craton in south Australia. Influence of sedimentary basins and plate boundaries. *Proceedings of the 11th IAGA Scientific Assembly*, Sopron, Hungary.

Thiel, S. & Heinson, G., 2013. Electrical conductors in Archean mantle—Result of plume interaction? *Geophysical Research Letters*, **40**, 2947-2952.

Thiel, S., Heinson, G. & White, A., 2005. Tectonic evolution of the southern Gawler Craton, South Australia, from electromagnetic sounding. *Australian Journal of Earth Sciences*, **52**, 887-896.

Thiel, S., Reid, A.J., Heinson, G. & Brand, K., in prep. Mantle-derived fluid flux controls Olympic Dam-style Fe oxide-Cu-Au mineralisation.

Tiddy, C. J. & Giles, D., 2020. Suprasubduction zone model for metal endowment at 1.60-1.57 Ga in eastern Australia. *Ore Geology Reviews*, 103483.

Tietze, K. & Ritter, O., 2013. Three-dimensional magnetotelluric inversion in practice—the electrical conductivity structure of the San Andreas Fault in Central California, *Geophysical Journal International*, **195**(1), 130–147, https://doi.org/10.1093/gji/ggt234.

Tietze, K., Ritter, O. & Egbert, G.D., 2015. 3-D joint inversion of the magnetotelluric phase tensor and vertical magnetic transfer functions. *Geophysical Journal International*, **203**(2), 1128–1148, https://doi.org/10.1093/gji/ggv347.

Wade, C. E., Reid, A. J., Wingate, M. T., Jagodzinski, E. A. & Barovich, K., 2012. Geochemistry and geochronology of the c. 1585 Ma Benagerie Volcanic Suite, southern Australia: Relationship to the Gawler Range Volcanics and implications for the petrogenesis of a Mesoproterozoic silicic large igneous province. *Precambrian Research*, **206**, 17-35.

Wade, C.E., Payne, J.L., Barovich, K.M. & Reid, A.J., 2019. Heterogeneity of the sub-continental lithospheric mantle and `non-juvenile' mantle additions to a Proterozoic silicic large igneous province. *Lithos*, **340-341**, 87-107.

Weidelt, P., 1973. The Inverse Problem of Geomagnetic Induction, *Geophysical Journal International*, **35**(1-3). 379, https://doi.org/10.1093/gji/35.1.379

Weidelt, P., 1999. 3-D Conductivity Models: Implications of Electrical Anisotropy," *Geophysical Developments Series:* 119-137. https://doi.org/10.1190/1.9781560802154.ch8

White, A. & Milligan, P. 1984. A crustal conductor on Eyre Peninsula, South Australia, *Nature*, **310**, 219-222.

Wingate, M.T., Campbell, I.H., Compston, W. & Gibson, G.M., 1998. Ion microprobe U–Pb ages for Neoproterozoic basaltic magmatism in south-central Australia and implications for the breakup of Rodinia. *Precambrian Research*, **87**(3–4), 135–159.

Yang, B., Egbert, G.D., Kelbert, A. & Meqbel, N., 2015. Three-dimensional electrical resistivity of the north-central USA from EarthScope long period magnetotelluric data. *Earth and Planetary Science Letters*, **422**, 87-93.

Yoshino, T. & Katsura, T., 2013. Electrical Conductivity of Mantle Minerals: Role of Water in Conductivity Anomalies. *Annual Review of Earth and Planetary* Sciences, **41**, 605-628.

https://doi.org/10.1146/annurev-earth-050212-124022

Yoshino, T., Matsuzaki, T., Yamahista, S. & Katsura, T., 2006 Hydrous olivine unable to account for conductivity anomaly at the top of the asthenosphere. *Nature*, **443**, 973-976.

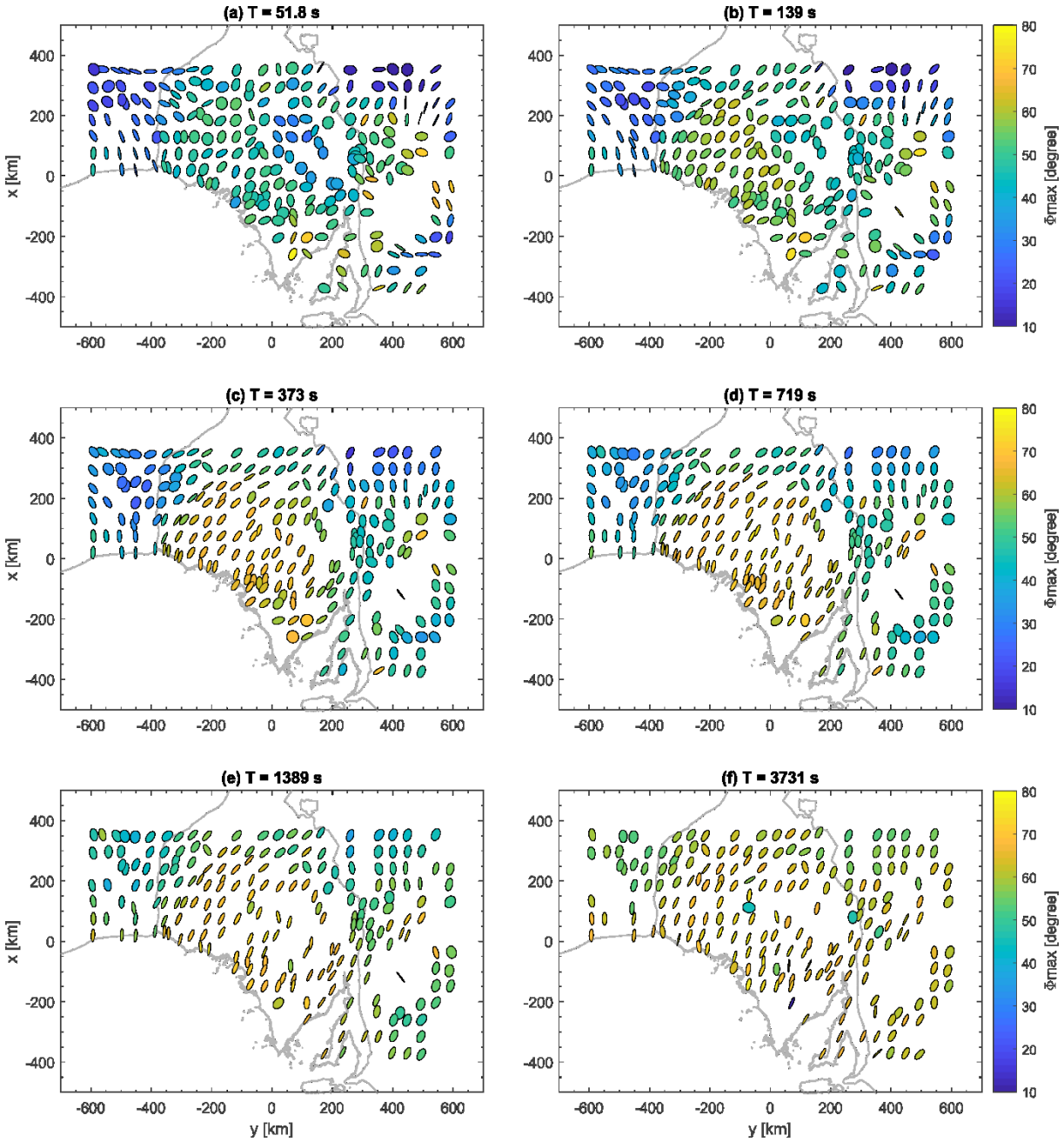

Figure 1: The field data set. Maps of phase tensor ellipses for various periods. Ellipses are normalised and coloured with the value of phimax. Grey outline shows onshore extent of the Gawler craton (Korsch & Doublier 2015).

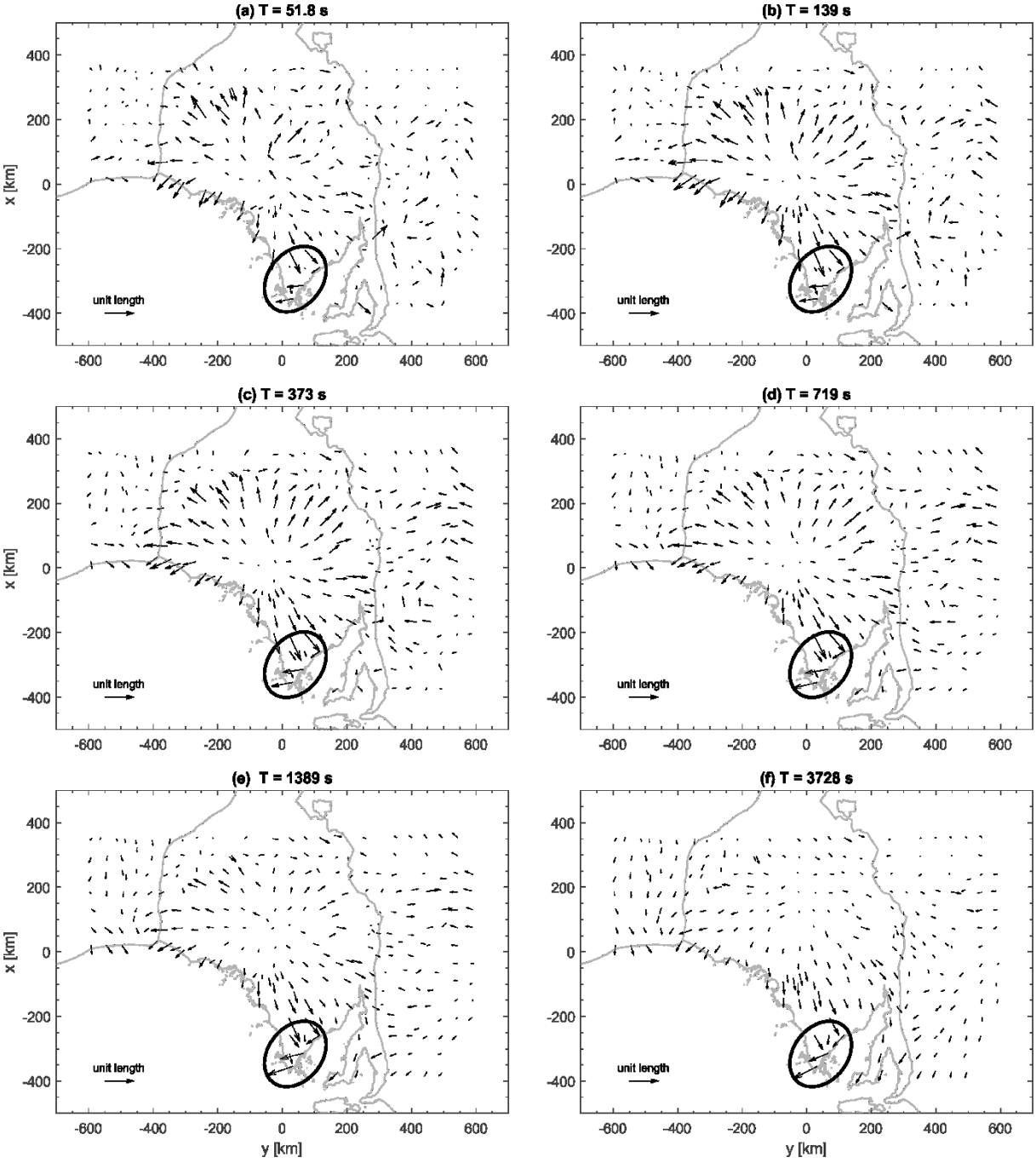

Figure 2: The field data set. Maps of induction vectors (real parts) in Parkinson convention for various periods. Black ellipse marks reversal of induction arrows across the Eyre Peninsula conductor (see main text). Grey outline shows illustrates extent of Gawler craton (onshore).

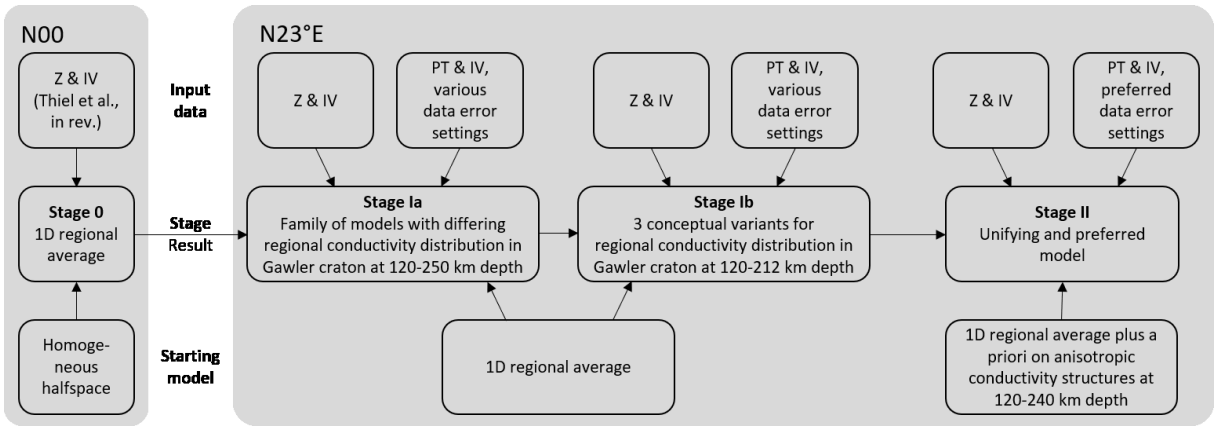

Figure 3: Flow chart of the inversion process, consisting of three stages with different starting models and input data. N00 and N23°E: x-axis of modelling coordinate system points towards N00° (geographic North) and N23°E, respectively; Z: impedances, IV: induction vectors, PT: phase tensors.

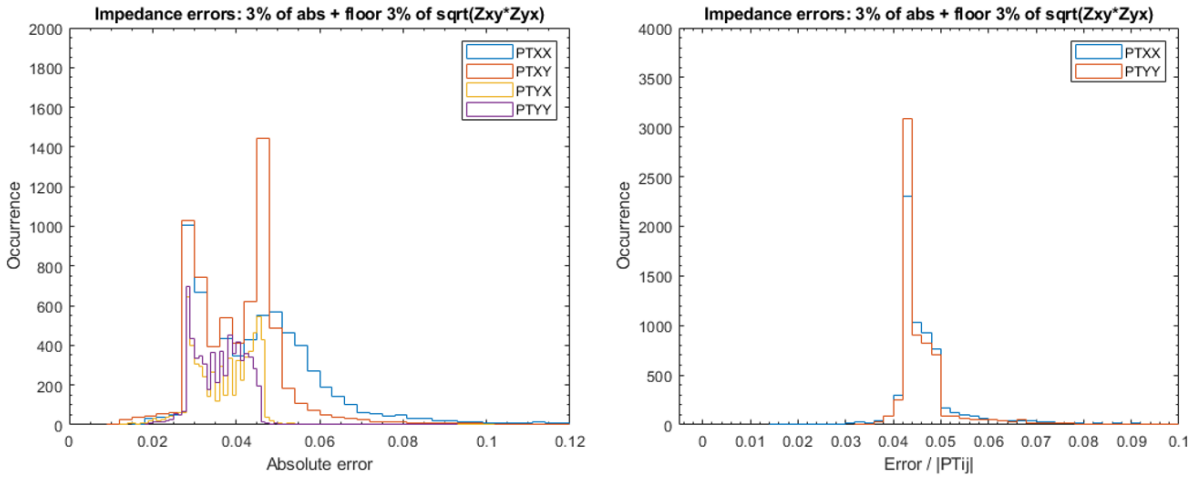

Figure 4: Distribution of phase tensor errors obtained from error propagation (from impedances).

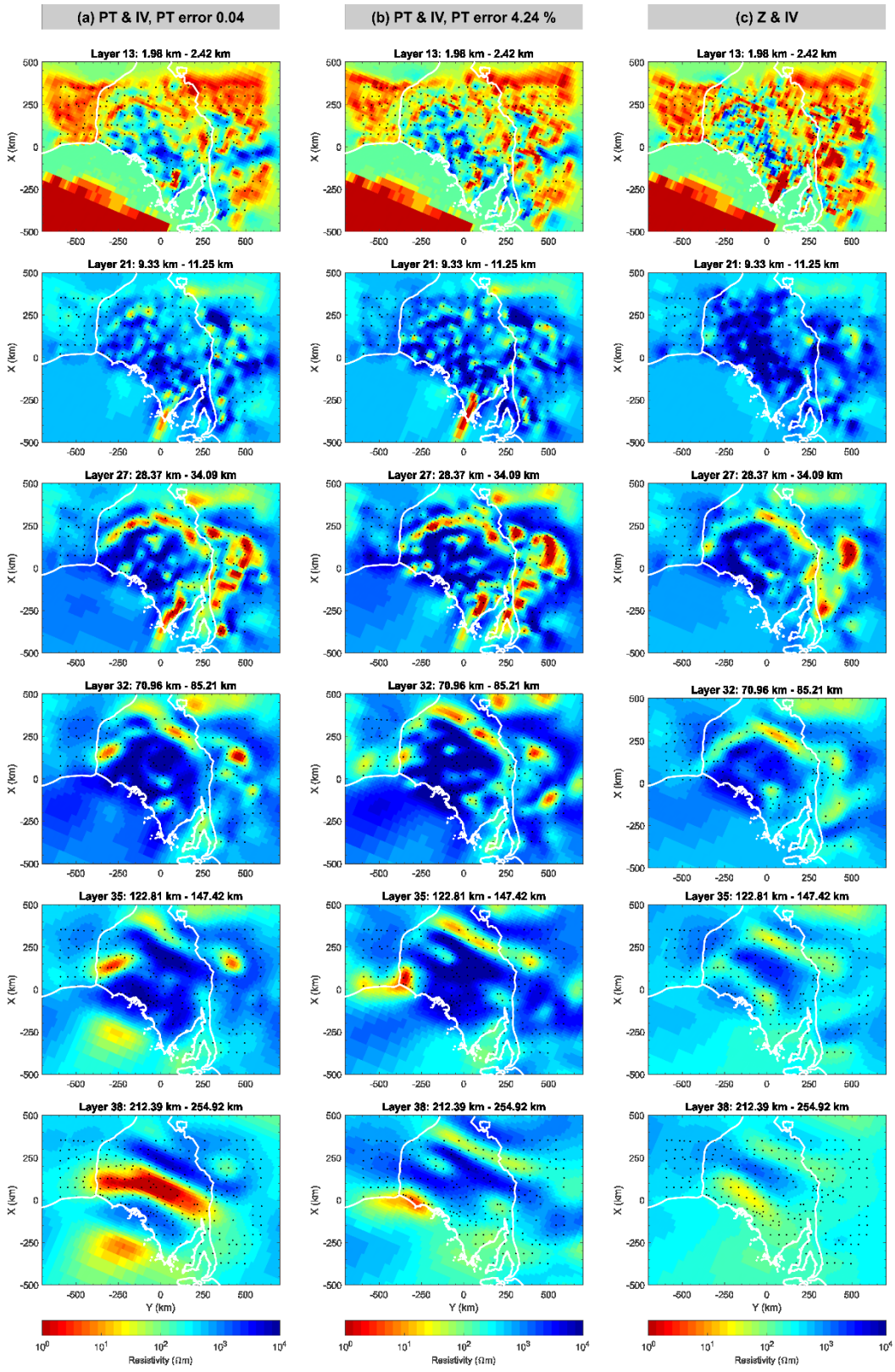

Figure 5: Resistivity models of the field data obtained from joint inversion of (a)-(b) phase tensors/ induction vectors and (c) impedances/induction vectors. (a) Phase tensor errors were set to 0.04, (b) phase tensor errors were set to 4.24 % in combination with an absolute floor of 0.025. White lines indicate coastline and outline of Gawler Craton. See main text for inversion details.

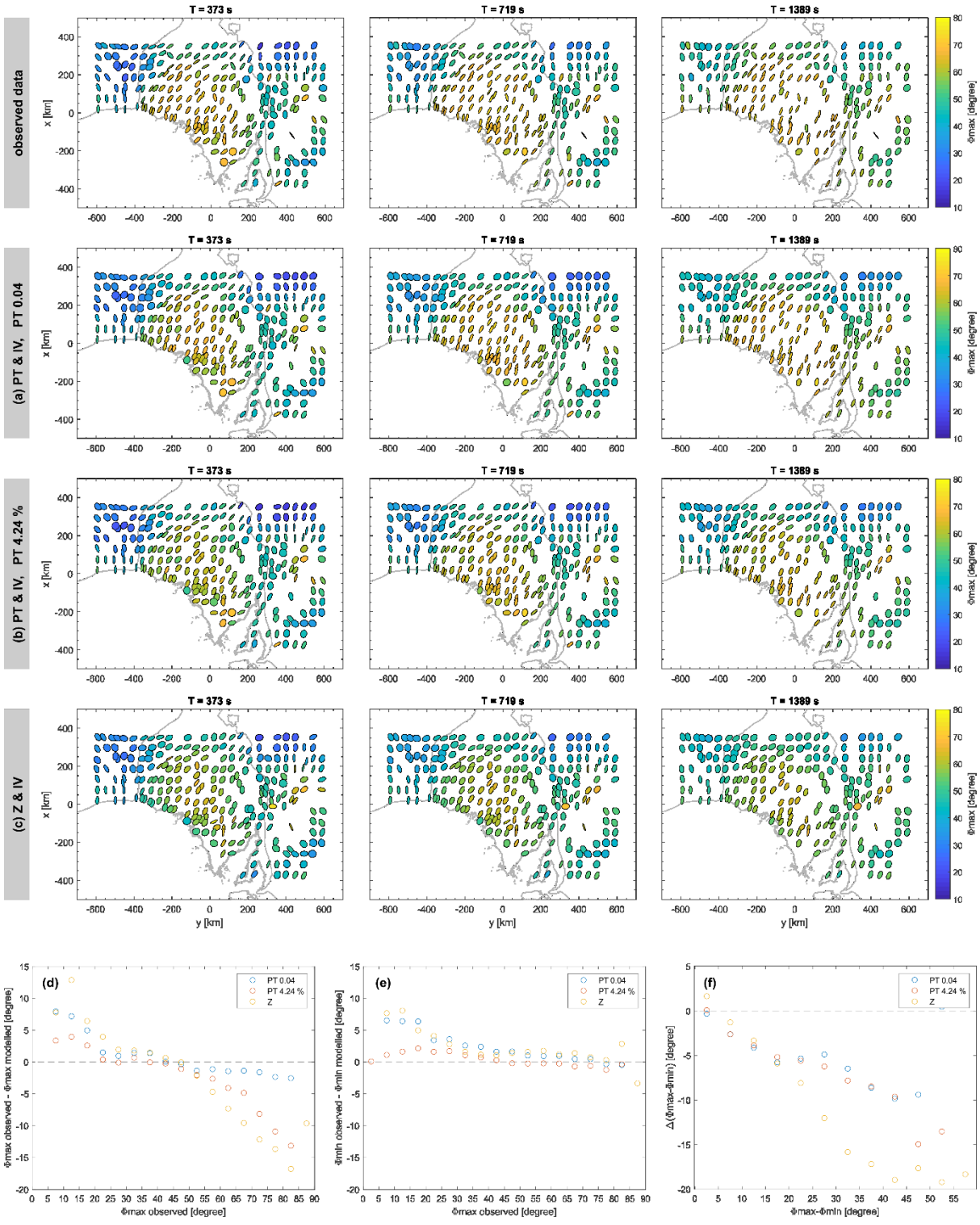

Figure 6: (a)-(c) Responses of inversion models of Figs 5(a)-(c). (d)-(f) Median difference between observed and modelled phase tensor parameters: (d) phimax, (e) phimin, and (f) phimax-phimin. Median difference was estimated over data points with (d)-(e) observed phimax values between]0 n*5] for n=1…18 and (f) observed phimax-phimin values between]0 n*5] for n=1…18. Grey dashed line marks an ideal data fit.

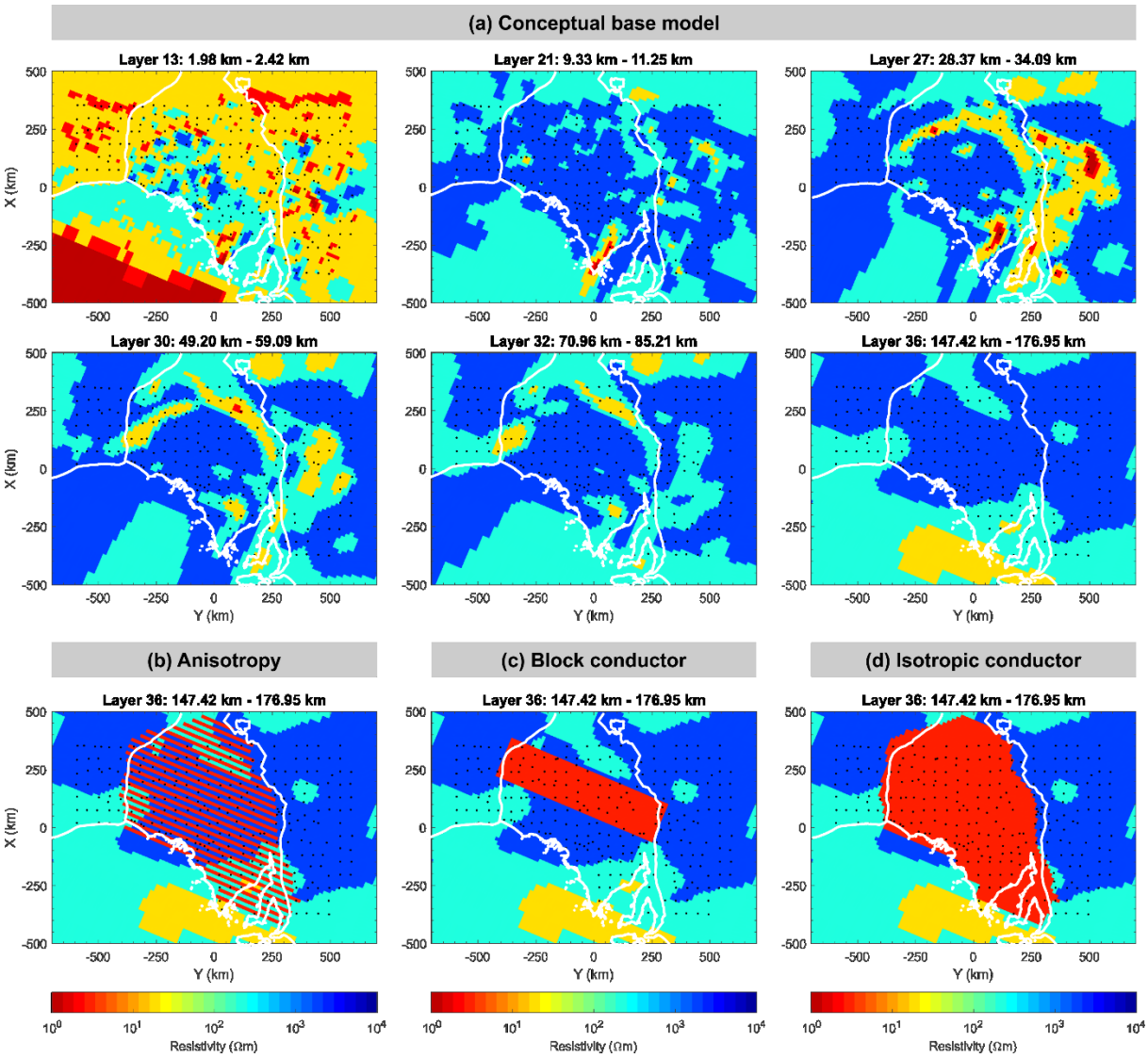

Figure 7: Conceptual 3D model. (a) Base model. (b)-(d) Variants of base model; (b) anisotropic Gawler base, (c) block conductor, (d) isotropic Gawler base.

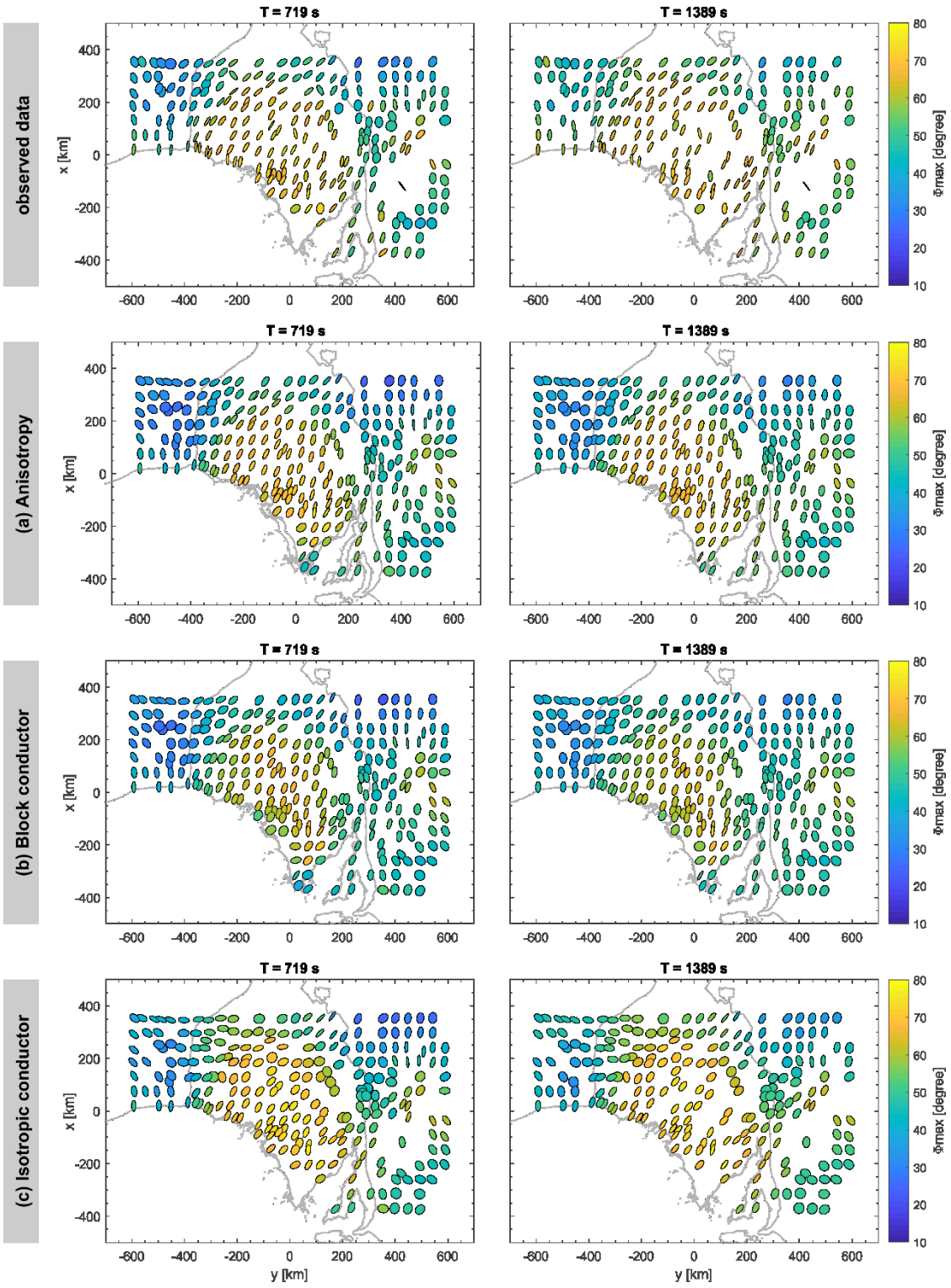

Figure 8: Phase tensor responses produced by the three variants of the conceptual models (cf. Figs 7b-d) compared to observed data. Phase tensors are shown as normalised ellipses coloured with the phase tensor maximum phase (phimax). (a) Anisotropic Gawler base, (b) block conductor, (c) isotropic conductor at Gawler base.

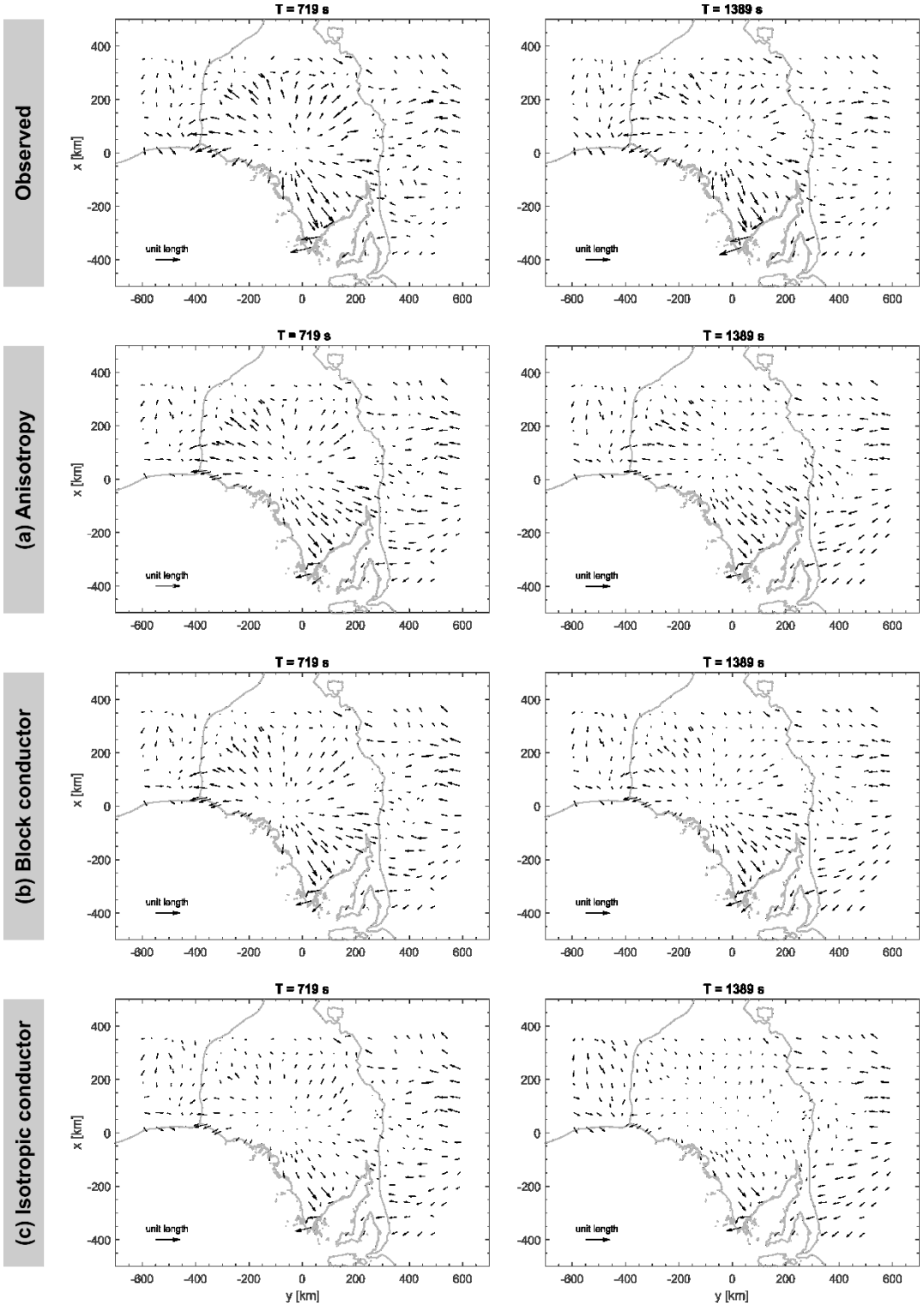

Figure 9: Induction vectors produced by the three variants of the conceptual models (cf. Figs 7b-d) compared to observed data: (a) Anisotropic Gawler base, (b) block conductor, (c) homogeneous conductor at Gawler base.

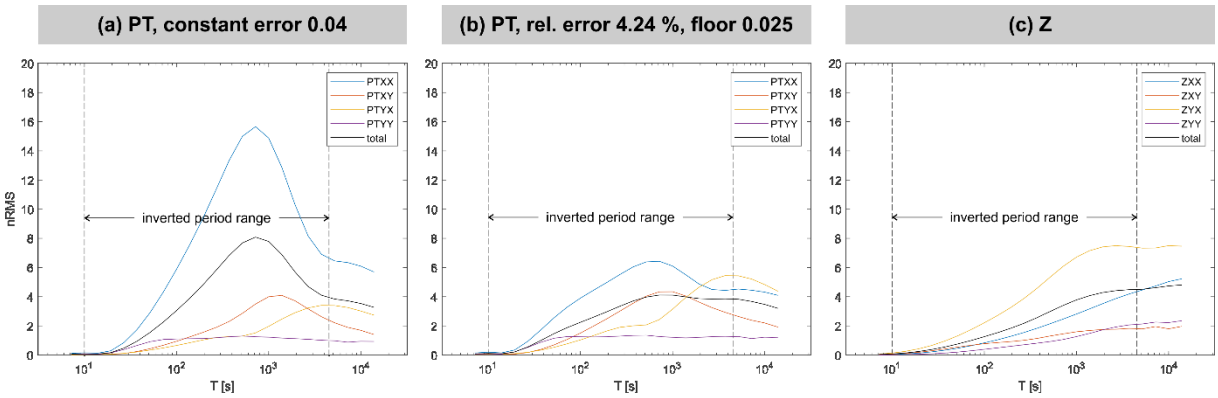

Figure 10: Comparison of responses between conceptual model with anisotropic Gawler and the base model for different data types and data error settings. Difference between model responses displayed as normalises RMS (nRMS) vs period. (a) phase tensor with constant error of 0.04, (b) phase tensor with errors of 4.24 % and a constant floor of 0.025, (c) impedances with errors of 3 % and a floor of 3 % of sqrt(|Zxy*Zyx|) for the diagonal elements Zxx and Zyy.

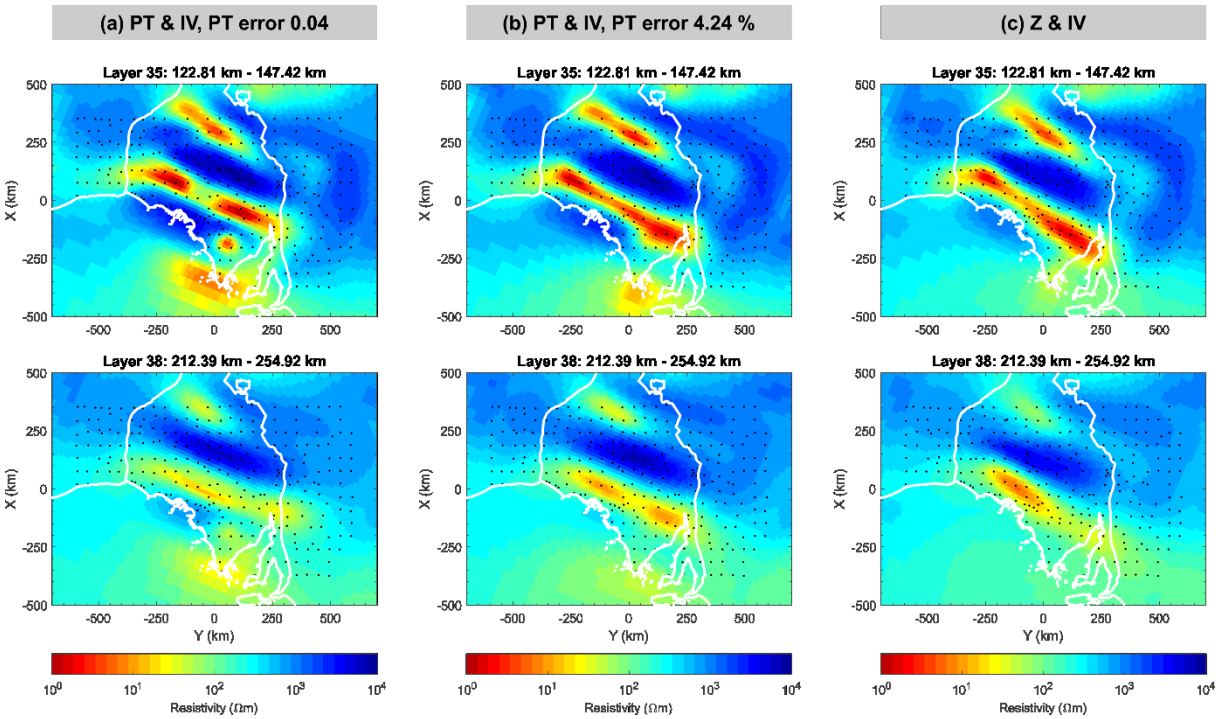

Figure 11: Resistivity models for the conceptual data set of the anisotropic Gawler base (true model displayed in Figs 7a-b) using joint inversion of phase tensors or impedances and vertical magnetic transfer function. (a) phase tensors with constant errors of 0.04; (b) phase tensors using relative data errors; (c) impedances.

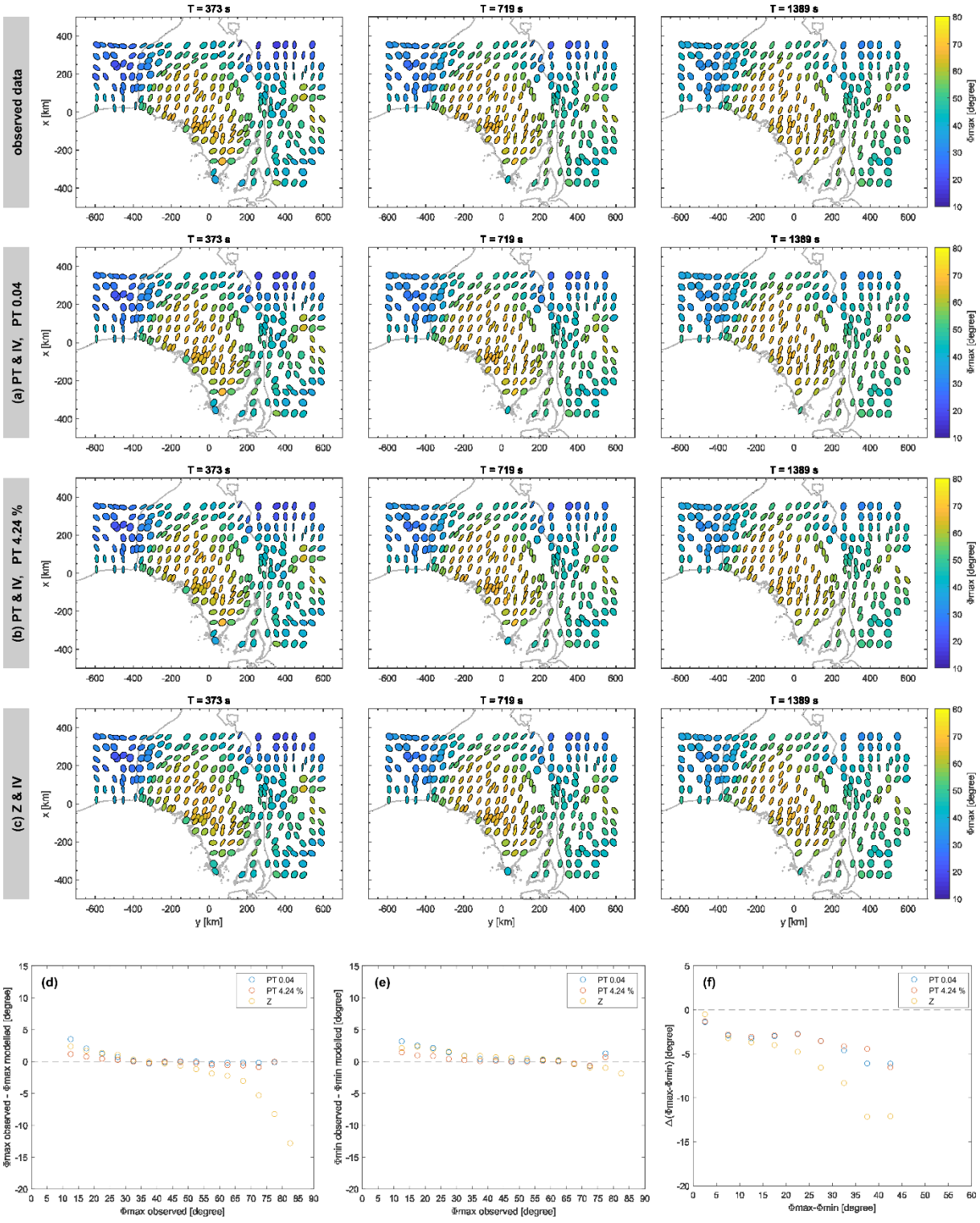

Figure 12: (a)-(c) Responses of inversion models of Figs 11(a)-(c). (d)-(f) Median difference between observed an modelled phase tensor parameters: (d) phimax, (e) phimin, and (f) phimax-phimin. Median difference was estimated over data points with (d)-(e) observed phimax values between]0 n*5] for n=1…18 and (f) observed phimax-phimin values between]0 n*5] for n=1…18. Grey dashed line marks an ideal data fit.

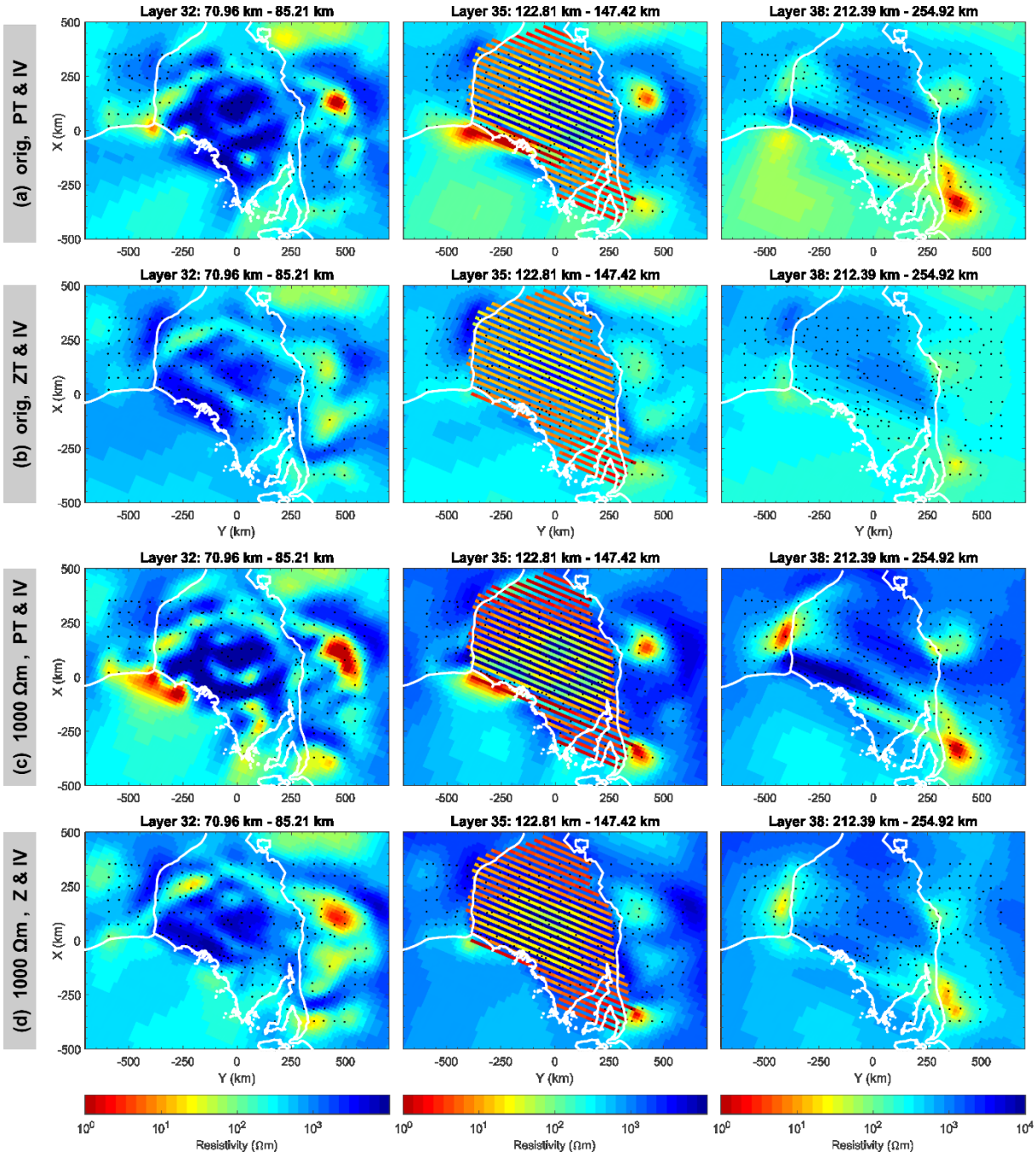

Figure 13: Resistivity models of the field data obtained for inversions with a priori information. (a)-(b): 1D layered halfspace with 3 Ωm lamellae at depths of 120-210 km. (a) Joint inversion of phase tensors (constant error of 0.04) and induction vectors, (b) joint inversion of impedances and induction vectors. (c)-(d): Resistivities of the 1D layered halfspace were increased to 1000 Ωm at depths > 120 km before adding same lamellae as in (a)-(b). (c) Joint inversion of phase tensors and induction vectors, (b) joint inversion of impedances and induction vectors.

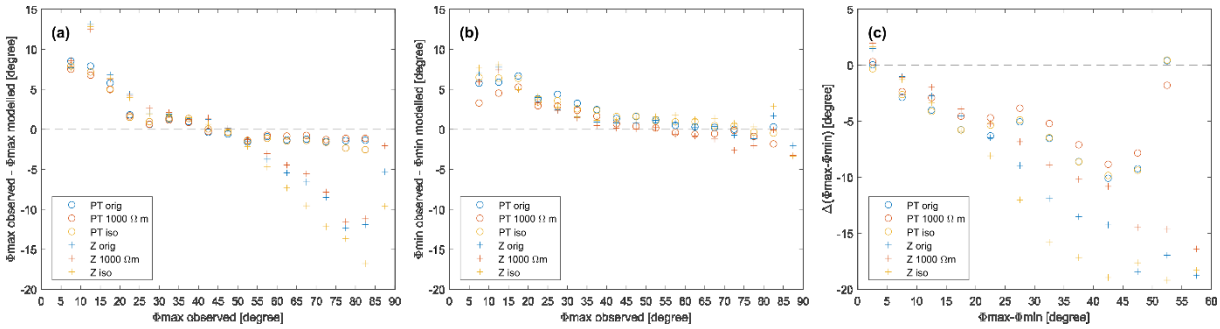

Figure 14: Fit of phase tensor parameters for inversion models displayed in Figs 13(a)-(d) and Figs 5(a) and (c). (a)-(c) Median difference between observed and modelled values of (a) phimax, (b) phimin, and (c) phimax-phimin. Median was estimated over data points with (a)-(b) observed phimax values between]0 n*5] for n=1…18 and (e) observed phimax-phimin values between]0 n*5] for n=1…18. Grey dashed line marks an ideal data fit.

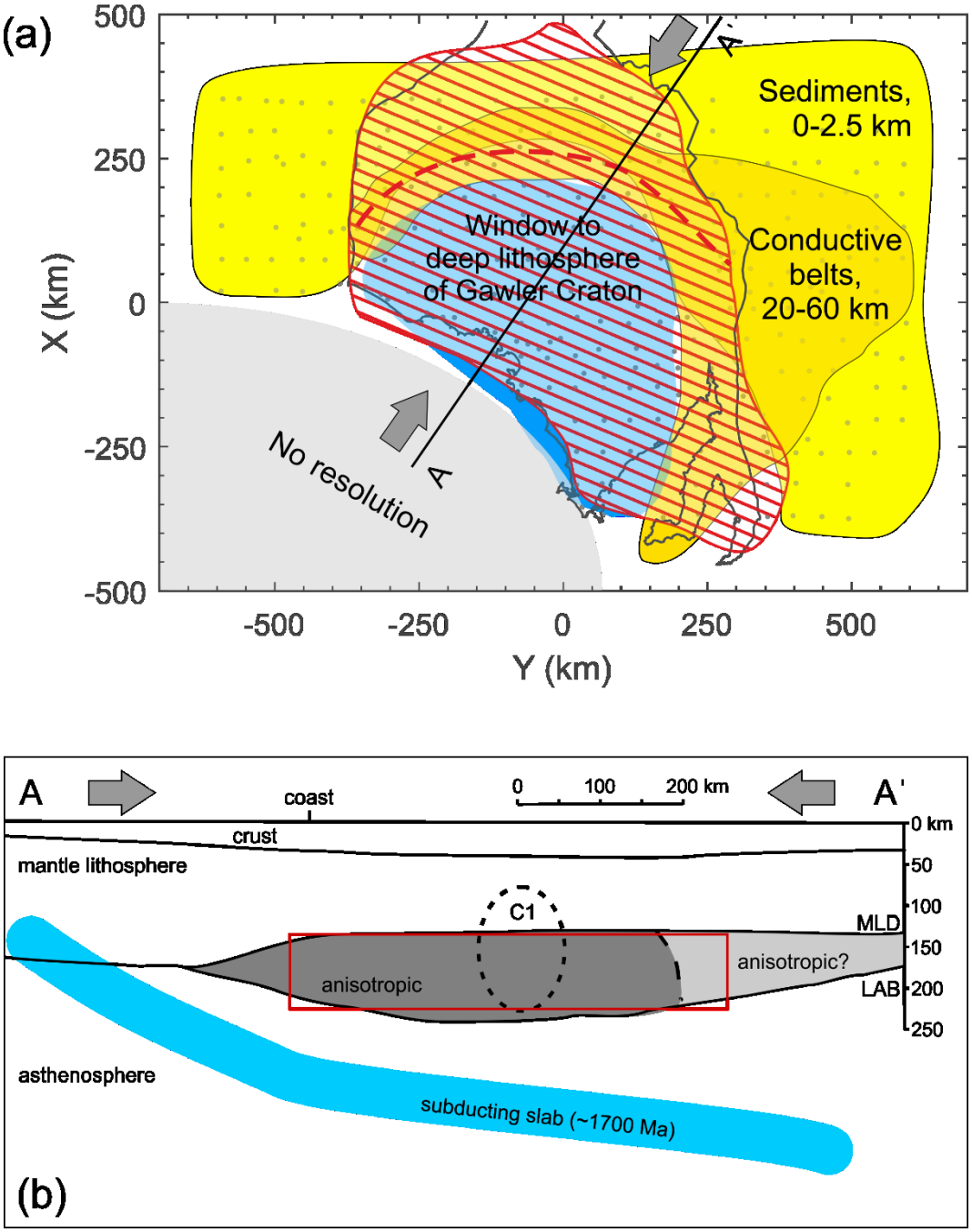

Figure 15: Interpreted results. (a) Map view. Grey line marks onshore extent of Gawler Craton. Red hatched area marks extent of anisotropic body (cf. Figs 7a and 13); hatching is parallel to the electrically conductive direction. Yellow shading indicates areas with penetration depths of MT signals limited to 70-100 km depth due to presence of significant amounts of conductive material between 0 and 60 km depth. Highly resistive material in the centre of the Gawler Craton provides sensitivity to > 200 km depth (blue shading). (b) Cross-sectional view, see (a) for profile location. Figure redrawn and modified from Skirrow *et al.* (2018). The red outline marks location of anisotropic body used in modelling studies. C1 conductive zone imaged by Thiel & Heinson (2013), MLD mid-lithospheric discontinuity, LAB lithosphere-asthenosphere boundary. Grey arrows in (a) and (b) mark compressional direction related to subduction between ~1.7 and 1.5 Ga (Skirrow *et al.* 2018). See main text for details.

SUPPLEMENTARY MATERIAL:

S1 Inversion of the Gawler data set in a different coordinate system

Analogue to results shown in Figure 5, the Gawler data set was inverted in a coordinate system with the x-axis pointing to N22°W, i.e. at an angle of 45° to the original orientation. In order to keep the model mesh at manageable size, a horizontal discretisation of 20 km x 20 km was chosen in the central area covered with sites; the new model mesh consists of 75 × 80 × 55 cells including padding cells. Vertical discretisation is the same as for results in Figure 5. Accordingly, the 1D layered resistivity structure of the starting model was maintained. But 3D a priori conductivity features, namely the sea water and the sediments, were remapped. Data errors were recalculated in the new coordinate system using the same parameters as in section 4.1. All other inversion parameters are the same as described in section 4.1. The resulting models are shown in Figure S1.

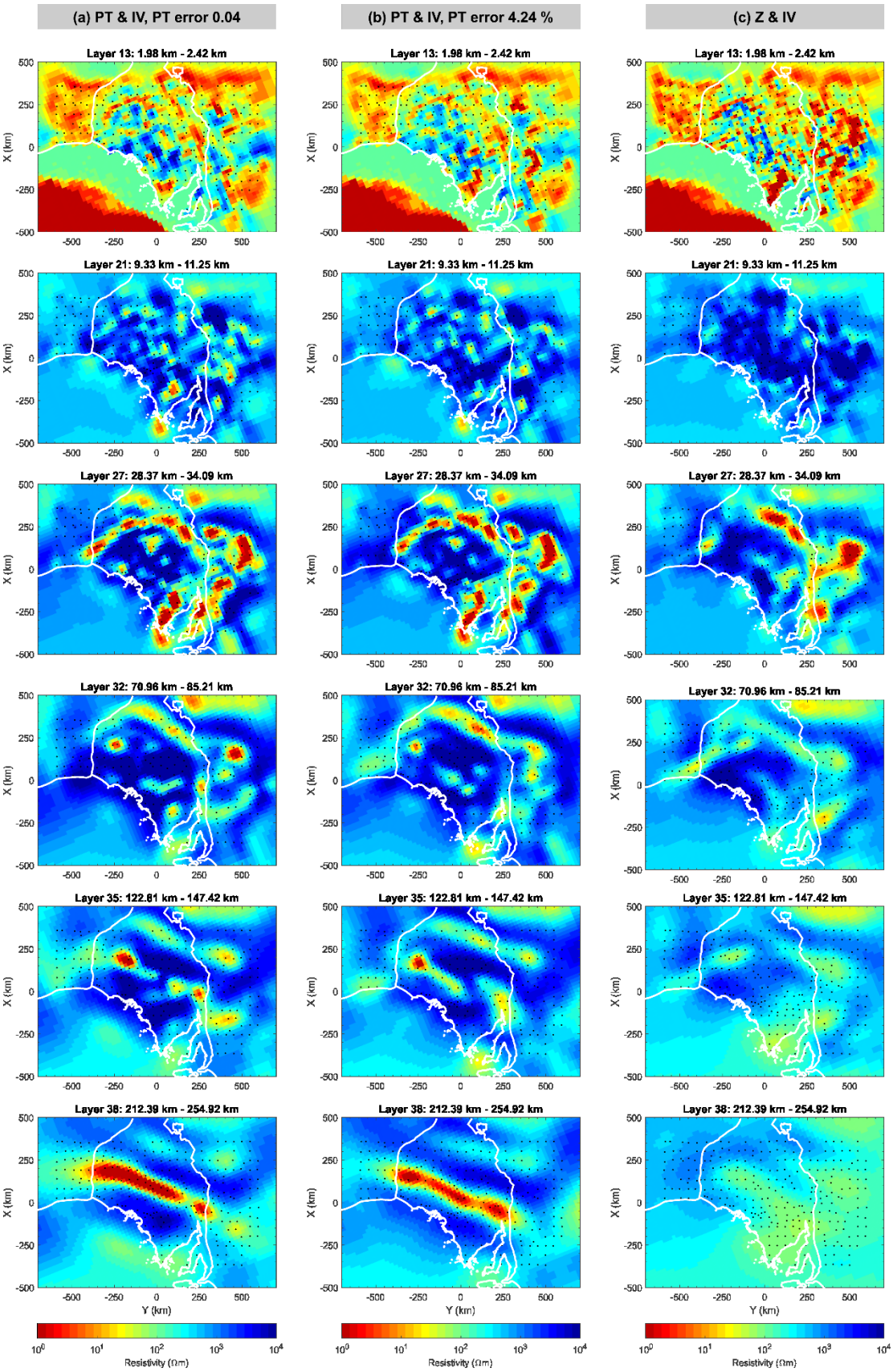

Fig. S1: Same as Figure 5, but using a coordinate system with *x* pointing to N22°W, i.e. at an angle of 45° from the original orientation. Inversions in (a)-(c) reached nRMS values of 3.47, 3.25 and 4.10, respectively.

S2 Reference model for the conceptual model

The inversion model in Figure S2 was obtained inverting the Gawler field data set as phase tensors and induction vectors and using errors of 5 % and a floor of 0.04 for phase tensors and 0.03 for induction vectors. This model was used to derive the conceptual base model as described in section 4.2.

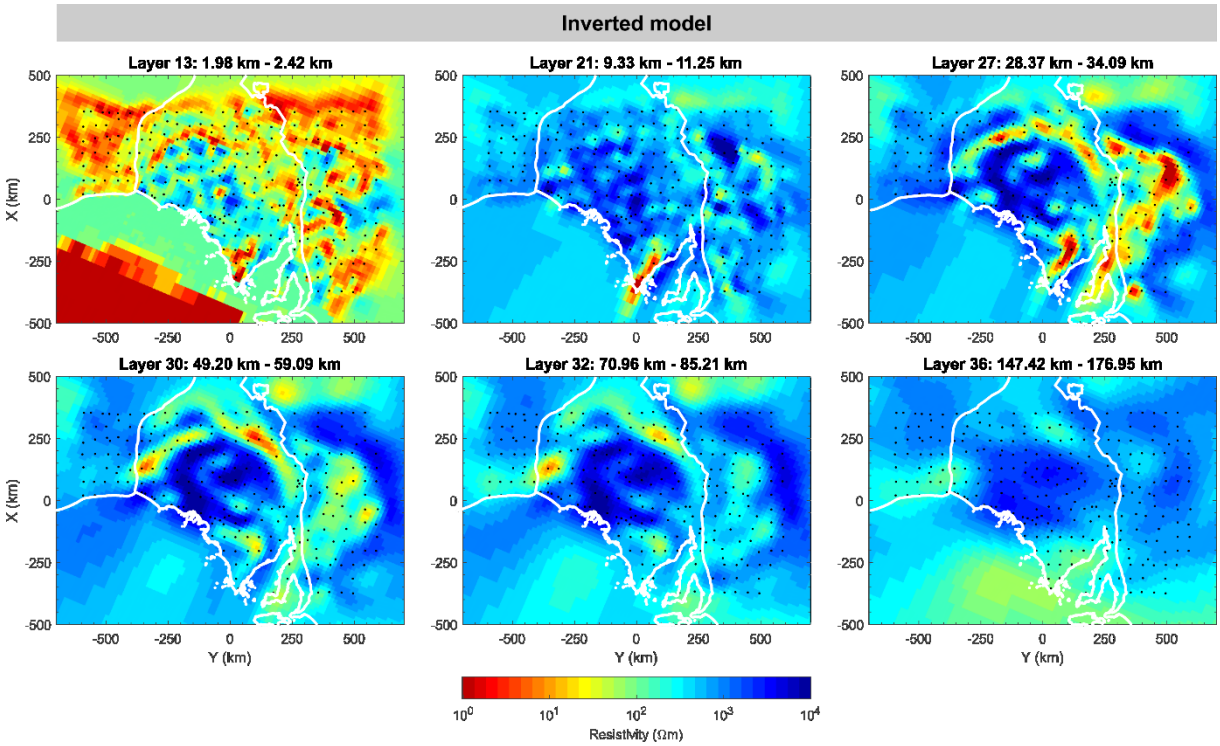

Fig. S2: Same as Figure 5a-b, but phase tensor errors were set to 10 % (Φxx, Φxy) and 5 % (Φyx, Φyy) in combination with an absolute error floor of 0.04.